RICE UNIVERSITY

A Method to Compute Three Dimensional Magnetospheric Equilibria with Dipole Tilt and its Application in Estimating Magnetic Flux Tube Volume

by

Liheng Zheng

A Thesis Submitted
in Partial Fulfillment of the
Requirements for the Degree

Master of Science

Approved, Thesis Committee:

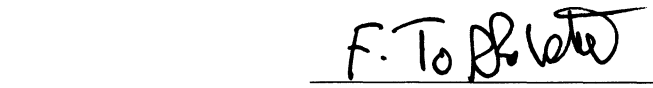

Frank R. Toffoletto, Chair
Professor of Physics and Astronomy

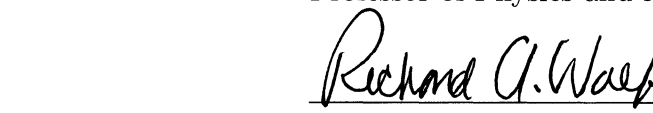

Richard A. Wolf
Professor Emeritus of Physics and Astronomy

Rui-Rui Du
Professor of Physics and Astronomy

Houston, Texas

May, 2011

Abstract

A Method to Compute Three Dimensional Magnetospheric Equilibria with Dipole Tilt and its Application in Estimating Magnetic Flux Tube Volume

by

Liheng Zheng

In this thesis we describe a new version of a magneto-friction model, which was developed for computing the magnetospheric equilibrium that includes an arbitrary Earth's dipole tilt and interplanetary magnetic field. We also describe the algorithms of this new friction code that trace magnetic field lines, locate the neutral sheet, and identify the magnetopause. In addition, we present a generalized theory for calculating magnetic flux tube volume in the magnetotail, in an attempt to generalize the Wolf [2006] empirical formula, and describe a method for estimating flux tube volume from measurements at geosynchronous orbit. This new method has been tested against various equilibrated magnetospheres generated by the new friction code. Although still incomplete, the method exhibits promising features, and is to be completed in the future.

Acknowledgements

First and foremost, I would like to thank my thesis advisor Dr. Frank Toffoletto for his guidance and inspiration on work leading to this thesis. I am grateful for his patience and the freedom he gave to me during my research. I have benefited a lot from our weekly discussion covering from physics ideas, to research methods, and to every trivial that teaches me to be a more accomplished person. He guided me into the realm of space physics.

I feel fortune to have my fellow office-mates Jian Yang and Bei Hu. Their interesting discussions, comments, and helpful suggestions make the office an enjoyable place to work. My appreciation goes out to Asher Pembroke and Yen-Fei Chen for teaching me to use LaTeX to complete this thesis.

At last, I would like to express my gratitude to my family and my girl friend Yuhua Feng for their sustaining and warm support on my study abroad.

Contents

Illustrations

Tables

Chapter 1

Introduction

This dissertation describes the recent development of a new version of the magneto-friction code (the friction code) and its application for finding a better estimate of the magnetic flux tube volume in the magnetosphere. The friction code is a three dimensional numerical algorithm that calculates the force-balanced states of the magnetosphere, by adding an artificial frictional term into the magnetohydrodynamic (MHD) momentum equation to dissipate potential energy of the system. This relaxation mechanism for plasma was first proposed by *Chodura and Schlüter* [1981] [13], then developed into a magnetospheric equilibrium solver by *Hesse and Birn* [1993] [17] and subsequently by *Lemon et al.* [2003] [22]. The previous version of the friction code simplifies the system by assuming that the Earth's magnetic dipole axis is perpendicular to the Sun-Earth direction, and that the interplanetary magnetic field (IMF) is completely aligned with the dipole axis. Viewed from the Geocentric Solar Magnetospheric coordinate system (GSM, see Appendix 3 in *Kivelson and Russell* [1995] [19]), this dipole axis configuration means the dipole tilt angle is zero. These symmetries greatly simplify the geometry involved in the problem and therefore reduce the amount of computation. In the new version of the friction code, all these symmetric restrictions are removed, making it capable of dealing with more realistic and more complicated magnetosphere configurations, and able to be used in the study

on how the asymmetries will affect the magnetospheric plasma convection.

Chapter 1 of this dissertation briefly reviews the magnetospheric equilibrium problem, explaining why it is an important and interesting problem in the study of magnetospheric physics. Previous work on this problem, both theoretical and numerical, are also introduced in this chapter. The new version of the friction code is presented in detail in Chapter 2. The organization of this chapter is structured by describing the friction code, followed by an assessment of accuracy and a discussion on the ongoing work on the PV^{γ} correction. Chapter 3 describes the application of the new friction code to estimating the magnetic flux tube volume, which is a physical quantity that cannot be measured directly by spacecraft but is crucial in the theory of magnetospheric plasma convection. Initial results and future work of this study are also discussed here. Chapter 4 summarizes the thesis.

1.1 The magnetosphere equilibrium problem

This section is intended to introduce the terminologies and basic equations of the magnetosphere equilibrium problem to the readers. Readers already familiar with this are welcome to skip this section and continue your reading from section 1.2 .

1.1.1 The magnetosphere

The region of space around the Earth (and other magnetized planets in the Solar system) is not empty but rather filled with large amount of freely-moving charged

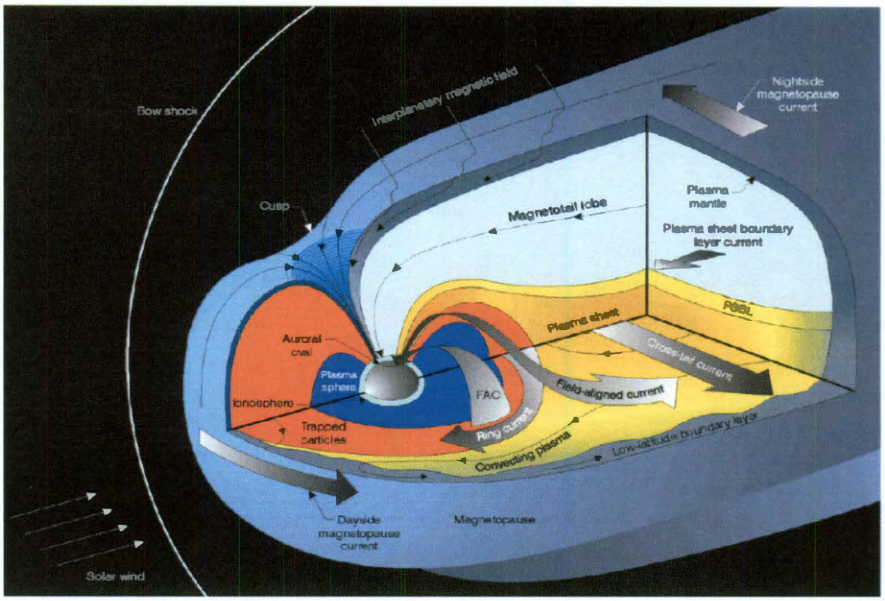

Figure 1.1 : Schematic illustration of the Earth's magnetosphere and its current systems. The figure was adopted from `http://www.physics.csbsju.edu/~jcrumley/364_2007/lectures/8-3/` on April 7, 2011.

particles called plasma. The sources are mainly from the solar wind and the result of ionization of neutral particles in Earth's high altitude atmosphere (thus named ionosphere). These particles drift and convect under the influence of the Earth's magnetic field, form current systems and in return affect the configuration of the magnetic field. The interaction between the solar wind and the magnetic field of the Earth produces a cavity around the Earth which is called the magnetosphere. Figure 1.1 gives a schematic illustration of the Earth's magnetosphere and the currents flowing within it. The boundary between the solar wind and the magnetosphere is called the magnetopause. The figure includes the region from near to the Earth to several tens of R_E downstream, the plasmasphere, the plasma sheet, and the north and south magnetotail lobes. The magnetopause, the polar cusps and the ionosphere

constitute the outer and inner boundaries of the magnetosphere. The central region of the plasma sheet, where magnetic field strengths are the weakest, is called the neutral sheet. If the magnetosphere is north-south symmetric, the neutral sheet is a plane coincident with the magnetic equatorial plane; but generally, it is a curved surface.

1.1.2 MHD equations

The basic equations delineating the magnetospheric plasma convection are the equations of ideal MHD. For isotropic pressure, they read,

$$\frac{\partial \rho}{\partial t} + \nabla \cdot (\rho \vec{v}) = 0 \tag{1.1}$$

$$\rho \frac{d\vec{v}}{dt} = \vec{J} \times \vec{B} - \nabla P \tag{1.2}$$

$$\frac{d}{dt}(\frac{P}{\rho^{\gamma}}) = 0 \tag{1.3}$$

$$\frac{\partial \vec{B}}{\partial t} = \nabla \times (\vec{v} \times \vec{B}) \tag{1.4}$$

$$\nabla \times \vec{B} = \mu_0 \vec{J} \tag{1.5}$$

where

$$\frac{d}{dt} = \frac{\partial}{\partial t} + \vec{v} \cdot \nabla \tag{1.6}$$

is the total time derivative with respect to a fluid element. γ in (1.3) is the adiabatic exponent, and is equal to 5/3 for the space plasma whose mass mainly comes from protons. Equations (1.1) through (1.3) are the MHD version of fluid equations of mass, momentum and energy, respectively. Equation (1.4) is a combination of Ohm's

law for a perfect conductor ($\vec{E} = -\vec{v} \times \vec{B}$) and Faraday's law. Equation (1.5) is Ampère's law with displacement current neglected, because fluid velocities are small compared to the speed of light. In addition, there are two Maxwell equations left: Gauss law equation is usually not solved because the perfect conductivity condition connects electric field $\vec{E}$ with magnetic field $\vec{B}$; whereas the divergence free condition for $\vec{B}$ is regarded as an initial condition.

A few comments need to be mentioned about the MHD equations. First, mathematically, it can be shown that the rate of change of the magnetic flux through a fluid element is

$$\frac{d\Phi}{dt} = \iint [\frac{\partial \vec{B}}{\partial t} - \nabla \times (\vec{v} \times \vec{B})] \cdot d\vec{\sigma} \tag{1.7}$$

in which $d\vec{\sigma}$ is the differential cross section of the fluid element. Equation (1.7) together with equation (1.4) indicate that the flux through a fluid element is invariant as the fluid flows, or in other words, the flux is "frozen-in" the fluid. If two fluid elements reside on the same magnetic field line at time t, they will reside on the same magnetic field line forever. One result of this "frozen-in flux" is that every field line is hence associated to and identified by the plasma that lies on it. The field line moves as the plasma frozen to it moves. Second, like in the case of unmagnetized fluid, "sound waves" can be inferred from the MHD equations; in addition, there are three independent modes of MHD waves, namely: the fast mode, the intermediate mode and the slow mode (according to their speeds). This is because in MHD waves, restoration force does not only come from thermal pressure P, but also magnetic

pressure $\frac{B^2}{2\mu_0}$ and magnetic tension force $\frac{B^2}{\mu_0}$ along field lines. The intermediate mode wave, also known as Alfvén wave, is analogous to the transverse wave in a stretched string, except that the "string" here is the magnetic field line and the tension is the magnetic tension force. When propagating along the field line, the Alfvén speed is given by

$$c_A^2 = \frac{B^2}{\mu_0 \rho} \tag{1.8}$$

A typical value of Alfvén speed in the inner magnetosphere is 1000 km/s. Fast mode propagates by compressing the plasma and the magnetic field in phase, and its speed writes

$$c_F^2 = c_s^2 + c_A^2 \tag{1.9}$$

where

$$c_s^2 = \frac{\gamma P}{\rho} \tag{1.10}$$

is the conventional sound speed. Slow mode, on the other hand, propagates by compressing the plasma and the magnetic field out of phase. However, the expression of the slow mode speed is more complicated than the other two by being related to the direction of the wave vector, and is not given here. [*Wolf*, unpublished manuscript [35].]

1.1.3 Magnetohydrostatic equilibrium and adiabatic convection

During quiet (and most) times in the magnetosphere, plasma convection speeds near the Earth are very small compared to the waves speeds, and the characteristic flow

times are thus very long compared to the travel time of a signal between the ionosphere and the equatorial plane. Physically, this means the plasma within a magnetic flux tube (which is the "tube" confined by a bundle of magnetic field lines having one end at the northern ionosphere and the other at the southern ionosphere) is continuously adjusted to the boundary conditions at the footprints of that flux tube on the ionosphere, and hence keeps in a force balanced state [*Vasyliunas*, 1970 [29]]. Mathematically, the hierarchy requires, in the MHD equations, $\vec{v}$ and quantities generated by $\frac{\partial}{\partial t}$ to be first order quantities compared to the zeroth order quantities pressure, density, current and magnetic field. Consequently, the inertial term $\rho\frac{d\vec{v}}{dt} = \rho\left(\frac{\partial\vec{v}}{\partial t} + (\vec{v}\cdot\nabla)\vec{v}\right)$ in the momentum equation (1.2) becomes a second order quantity and is negligible. This hierarchy casts the MHD equations into two sets of equations according to their orders. Equations (1.2), (1.5) and the magnetic divergence-free condition are of the order of unity:

$$\vec{J}\times\vec{B} = \nabla P \qquad O(1) \tag{1.11}$$

$$\nabla\times\vec{B} = \mu_0\vec{J} \qquad O(1) \tag{1.12}$$

$$\nabla\cdot\vec{B} = 0 \qquad O(1) \tag{1.13}$$

These equations constitute the magnetohydrostatic equilibrium problem. However, the equilibria described by (1.11), (1.12) and (1.13) are not static, because first order equations (1.1), (1.3) and (1.4) still remain; they describe the time-dependent processes:

$$\frac{\partial\rho}{\partial t} + \nabla\cdot(\rho\vec{v}) = 0 \qquad O(\epsilon) \tag{1.14}$$

$$\frac{d}{dt}(\frac{P}{\rho^\gamma}) = 0 \qquad O(\epsilon) \tag{1.15}$$

$$\frac{\partial \vec{B}}{\partial t} = \nabla \times (\vec{v} \times \vec{B}) \qquad O(\epsilon) \tag{1.16}$$

Therefore, the magnetospheric convection is modeled by a sequence of magnetospheric equilibrium configurations, and is so named "quasi-static" convection.

From equation (1.11), it is immediately seen that P is constant along magnetic field lines. Thus, pressure is entirely determined by its boundary values that are specified in a plane which is intersected by all field lines, for example the equatorial plane. For isotropic Maxwellian plasma, ρ is also constant along field lines. If we define "flux tube volume" as the volume of a flux tube with unit magnetic flux:

$$V = \int \frac{ds}{B(s)} \tag{1.17}$$

where s denotes field line arc length and the integral extends along a field line from its footprint in one ionosphere to the conjugate in the other, then the average density in that flux tube volume can be evaluated by

$$\rho_{av} = \frac{M}{V} \tag{1.18}$$

in which M is the total mass of plasma in V. Note, for infinitesimally thin flux tubes, we have $\rho_{av} \rightarrow \rho$. Assuming plasma is lossless during convection, M is conserved. Replacing (1.18) into (1.14) yields the continuity equation in terms of V, and we have rewritten the first order equations (1.14) and (1.15) in the following form [*Voigt and Wolf*, 1988 [31]]

$$\frac{\partial V}{\partial t} + (\vec{v} \cdot \nabla)V - V(\nabla \cdot \vec{v}) = 0 \tag{1.19}$$

$$\frac{\partial P}{\partial t} + (\vec{v} \cdot \nabla)P + \gamma P(\nabla \cdot \vec{v}) = 0 \tag{1.20}$$

Combining equations (1.19) and (1.20) gives the thermodynamic equation of state

$$\frac{d}{dt}(PV^{\gamma}) = 0 \tag{1.21}$$

which says the quantity PV^{γ} is conserved for a flux tube as it convecting from the magnetotail to the near Earth magnetosphere, around the Earth under gradient/curvature drift and toward the dayside magnetopause. In other words, the convection is adiabatic. The physical importance of PV^{γ} is also manifested in that it is related to the entropy of particles in a flux tube by [*Wolf et al.*, 2009 [34]]

$$\frac{S}{N} = \frac{3}{2}\ln(PV^{\gamma}) - \frac{3}{2}\ln(N^{\gamma}) - \Lambda' \tag{1.22}$$

where S is entropy, N is the total number of particles in the flux tube, and Λ' is an integral constant that depends only on the shape of the distribution function and particle mass. Therefore, under lossless assumption, entropy is conserved for a flux tube during convection.

1.1.4 Field aligned currents

The equilibrium problem not only provides self-consistent magnetic field and pressure for the magnetospheric convection calculation, but also contains information about the configuration of field aligned currents that flow between the magnetosphere and the ionosphere. In the logical loop for magnetosphere convection calculation first

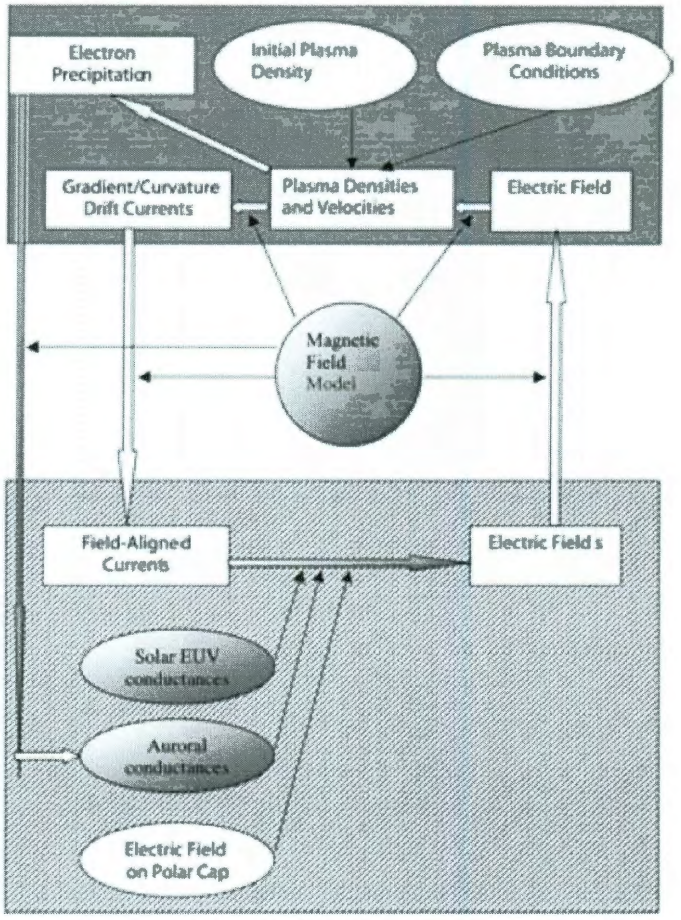

Figure 1.2 : Flowchart of the magnetosphere convection calculation. The central loop around the "Magnetic Field Model", connected by hollow arrows, is the main loop. The upper part of the figure represents magnetospheric quantities and the lower part ionospheric. Figure was adopted from *Sazykin* [2000] [24].

proposed by *Vasyliunas* [1970] [29], shown in Figure 1.2, field aligned currents play an essential role in coupling the magnetosphere with ionosphere.

Starting from equation (1.11), the current component perpendicular to $\vec{B}$ is easily calculated

$$\vec{J}_{\perp} = \frac{\vec{B} \times \nabla P}{B^2} \tag{1.23}$$

However, the component parallel with $\vec{B}$ is not simply given by dotting $\vec{B}$ on both sides of equation (1.12), but is derived from (1.23) and the requirement that $\nabla \cdot \vec{J} = 0$, and is expressed by Vasyliunas equation [for example, *Vasyliunas*, 1970 [29], or textbook draft by *Wolf*, [35]]:

$$\frac{J_{\parallel in}}{B_{in}} - \frac{J_{\parallel is}}{B_{is}} = \frac{\hat{b}}{B} \cdot (\nabla V \times \nabla P) \tag{1.24}$$

In (1.24), "*in*" and "*is*" stand for "northern ionosphere" and "southern ionosphere" respectively; $J_{\parallel}$ has positive value when current flow is in the $+\hat{b}$ direction, here $\hat{b}$ is the unit magnetic field direction vector. The right-hand side of Vasyliunas equation (1.24) can be evaluated at any point along a field line.

The Vasyliunas equation (1.24) implies a fundamental physical notation that, the field aligned currents are not only determined by the distribution of plasma, but also by the magnetic field topology via the flux tube volume. In addition, the contribution to the flux tube volume integral (1.17) mainly comes from the part of a field line where the field strength is weakest. Along a field line, the field is weakest in the tail region, especially in the tail plasma sheet. This means that the field configuration in the plasma sheet affects the gradient of the flux tube volume, and therefore the

field aligned current, in a crucial and sensitive way. This is why an equilibrium magnetosphere model satisfying the conditions (1.11) through (1.13) is desirable in this work. [*Voigt*, 1986 [32]]

1.1.5 Euler potentials and Grad-Shafranov equation

In this subsection, I will introduce the Euler potential representation of magnetic field, which is mostly useful in theoretical derivation, and the Grad-Shafranov equation whose solution describes the 2 dimensional magnetohydrostatic equilibrium.

The magnetic field can be written in the form

$$\vec{B} = \nabla\alpha \times \nabla\beta \tag{1.25}$$

which satisfies the divergence-free condition automatically. α and β are two scalars called Euler potentials. These scalars are constant along a field line, hence can be used as field line identifiers. In the case of Earth's dipole field, constant α surfaces are often chosen as the surface obtained from rotating a field line around the dipole axis, and constant β surfaces are then the meridian surfaces:

$$\alpha = -B_{EO}R_E^3\frac{\sin^2\theta}{r} \tag{1.26}$$

$$\beta = \phi \tag{1.27}$$

$\{r, \theta, \phi\}$ are the constituents of a spherical coordinate system; R_E is Earth's radius and B_{EO} is the magnetic strength in the equatorial plane on the Earth's surface.

Because pressure P is constant along a field line, it must be a function of α and β only, namely $P(\alpha, \beta)$. Inserting (1.25) into the force-balance equation (1.11), we

have

$$\vec{J} \times (\nabla\alpha \times \nabla\beta) = \frac{\partial P}{\partial \alpha}\nabla\alpha + \frac{\partial P}{\partial \beta}\nabla\beta \tag{1.28}$$

Given the arbitrary choice of Euler potentials under constraint (1.25), we find that equation (1.28) is satisfied by

$$\vec{J} \cdot \nabla\beta = +\frac{\partial P}{\partial \alpha} \tag{1.29}$$

$$\vec{J} \cdot \nabla\alpha = -\frac{\partial P}{\partial \beta} \tag{1.30}$$

We thus obtain the Euler potential equivalence of the equilibrium problem equations (1.11) to (1.13)

A special class of 2D equilibria can be derived from equations (1.29) and (1.30) if we assume there is no y coordinate dependence. Under the assumption

$$\alpha = A(x, z) \tag{1.31}$$

$$\beta = y \tag{1.32}$$

we find that P is only a function of A and equation (1.30) is identically satisfied. By comparing (1.31) with (1.25), it is clear that the flux function A is nothing but the y component (and the only non-zero component) of the magnetic vector potential. Equation (1.29) reduces to

$$J_y = \frac{dP}{dA} \tag{1.33}$$

Combining with Ampère's law (1.5) and Coulomb gauge $\nabla \cdot \vec{A} = 0$, we obtain from (1.33) the source-free Grad-Shafranov equation

$$\nabla^2 A + \mu_0 \frac{dP}{dA} = 0 \tag{1.34}$$

which is completely equivalent to the basic equations (1.11) through (1.13). We will return to this equation in the next section.

Interestingly, if Vasyliunas equation (1.24) is expressed in terms of Euler potentials, its right-hand side turns out to be the Jacobian of the coordinate transform from $\{\alpha, \beta\}$ to $\{V, P\}$

$$\frac{J_{\parallel in}}{B_{in}} - \frac{J_{\parallel is}}{B_{is}} = \frac{\partial V}{\partial \alpha}\frac{\partial P}{\partial \beta} - \frac{\partial V}{\partial \beta}\frac{\partial P}{\partial \alpha} \tag{1.35}$$

$$= \frac{D(V,P)}{D(\alpha,\beta)} \tag{1.36}$$

1.2 Review of previous work

1.2.1 2D linear Grad-Shafranov model

The 2D linear Grad-Shafranov model was the earliest and most widely used theoretical model in the treatment of magnetosphere equilibrium problem. The solution of the Grad-Shafranov equation (in a form slightly different from (1.34)) was first applied in seeking for stable confinement in tokamaks [*Freidberg*, 1982 [15]], and then applied to magnetospheric physics. Mathematically the tricky part of applying the Grad-Shafranov equation to the magnetosphere is that the Earth's dipole is a singular point in space. From the discussion in subsection 1.1.5, we have concluded that, under the assumption of y direction symmetry ($\partial/\partial y = 0$), $A(x, z)$ is the y component of the magnetic vector potential. Therefore,

$$B_x = -\frac{\partial A}{\partial z} \tag{1.37}$$

$$B_z = +\frac{\partial A}{\partial x} \tag{1.38}$$

Assuming Earth's dipole moment $\vec{M}_D$ pointing into the negative z direction, we can express the magnetization current caused by the dipole as

$$\begin{aligned} J_D &= \frac{1}{\mu_0}(\nabla \times \vec{M}_D)_y \\ &= \frac{1}{\mu_0} M_D \frac{\partial}{\partial x}\delta(x)\delta(z) \end{aligned} \tag{1.39}$$

Adding this magnetization current to the right-hand side of equation (1.33), we then obtain the inhomogeneous nonlinear equation

$$\nabla^2 A + \mu_0 \frac{dP}{dA} = -M_D \frac{\partial}{\partial x}\delta(x)\delta(z) \tag{1.40}$$

In order to solve equation (1.40) analytically, one usually linearizes it by assuming a special form of the pressure function

$$P(A) = \frac{k^2}{2\mu_0} A^2 \tag{1.41}$$

hence turning (1.40) into an inhomogeneous Helmholtz equation

$$(\nabla^2 + k^2)A = -M_D \frac{\partial}{\partial x}\delta(x)\delta(z) \tag{1.42}$$

Boundary conditions are often set so that the normal component of the magnetic field is zero on the boundaries, which mimics a closed magnetopause situation. Specifically for a simple rectangular boundary with dayside magnetopause at $x = b$ and tail magnetopause located at $z = \pm z_0$, the boundary conditions write

$$B_x(x = b) = 0, \quad B_z(z = \pm z_0) = 0 \tag{1.43}$$

The δ function on the right-hand side of (1.42) can be expanded by the complete set of eigenfunctions of the homogeneous Helmholtz equation. Consequently, the solution to the inhomogeneous problem (1.42) reads [*Voigt*, 1986 [32]]

$$A(x,z) = -\frac{M_D}{2}\sum_{n=1}^{\infty}\cos(\eta_n z)\cdot[\mathrm{sign}(x)F_n(x) - F_n(x-2b)] \tag{1.44}$$

with the eigenvalues

$$\eta_n = \frac{\pi}{2}\frac{(2n-1)}{z_0} \tag{1.45}$$

The eigenfunctions $F_n(x)$ have the form

$$F_n(x) = \exp(-\lambda_n|x|) \tag{1.46}$$

where the physical parameters λ_n are related to the pressure strength k and the eigenvalues η_n by

$$\lambda_n^2 = \eta_n^2 - k^2 \tag{1.47}$$

Note, the solutions with parameters $\lambda_n^2 < 0$ are still physically meaningful. They represent a different kind of equilibrium configuration [*Voigt and Wolf*, 1985 [30]]. Figure 1.3 shows a plot of the resultant field lines (contours of $A(x,z)$) from the solution (1.44).

Hilmer and Voigt [1987] [18] have used the homogeneous Grad-Shafranov model in their study on the effects of a finite B_y component upon magnetotail equilibria. In that work, to make the Grad-Shafranov equation linear, they had to assume that B_y was only a function of A. Using this simple model, they have also calculated field

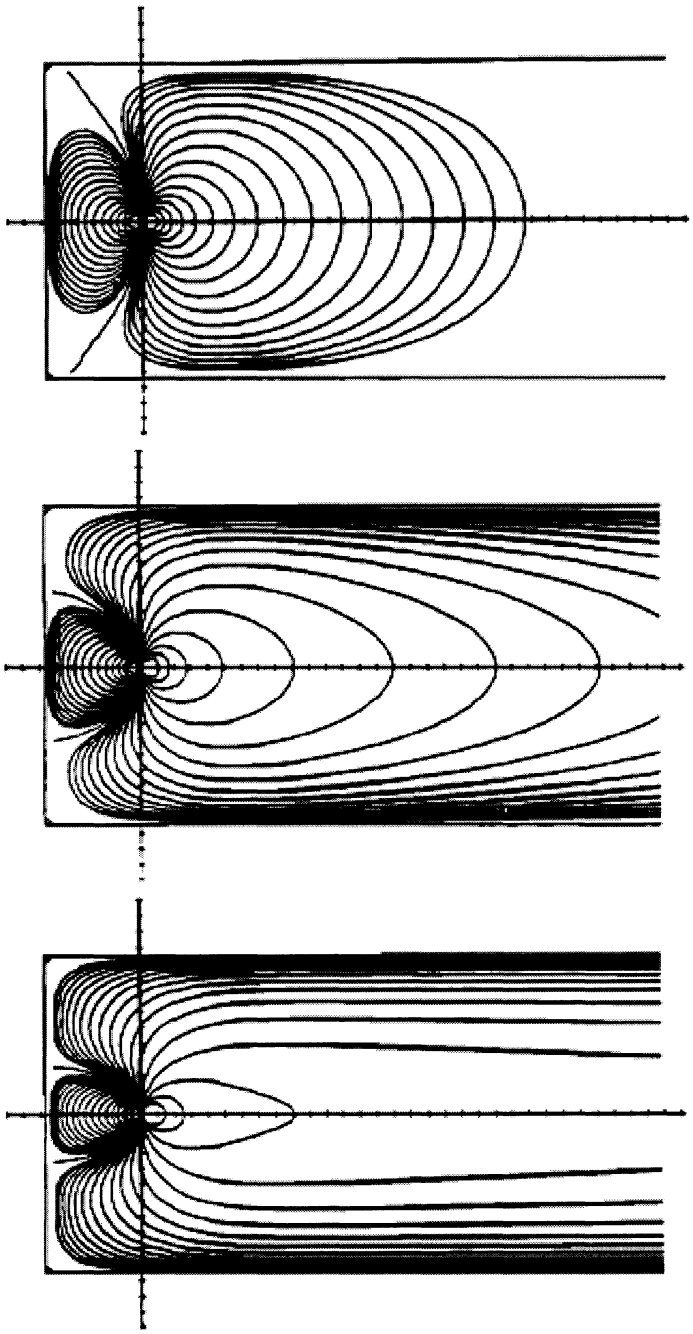

Figure 1.3 : Equilibrated magnetic field configurations from the solution to the linear Grad-Shafranov equation. From top to bottom, the plasma pressure varies between zero (vacuum case, $k = 0$) and the Harris sheet limit (zero B_z in the tail plasma sheet, $k = \eta_1$). Figure was adopted from Fig. 2 in *Voigt and Wolf* [1985] [30].

aligned currents caused by the finite B_y component and yielded qualitative agreement with observations.

1.2.2 3D asymptotic theory

Birn and collaborators examined the asymptotic properties of the Grad-Shafranov equation (1.34) in the tail region far from the Earth, and achieved an elegant 3D equilibrium theory [for example, *Birn et al.*, 1977 [8] and *Birn*, 1987 [3]]. In the far tail region, effects of the Earth's dipole becomes negligible, and the tail field lines are highly stretched. Therefore, *Birn* [1977] [8] assumed the "tail approximation" that

$$B_x, B_y, \partial/\partial z \sim O(1) \tag{1.48}$$

$$B_z, \partial/\partial x, \partial/\partial y \sim O(\epsilon) \quad \epsilon^2 \ll 1 \tag{1.49}$$

In the 2D case [*Birn et al.*, 1975 [7]], under these approximations, the Grad-Shafranov equation (1.34) reduces to

$$\frac{\partial^2 A}{\partial z^2} + \mu_0 \frac{dP}{dA} = 0 \tag{1.50}$$

Multiplying the left-hand side of this equation by $\dfrac{\partial A}{\partial z}$, we find that it is converted to an exact derivative with respect to z, and hence can be integrated once and yields

$$\frac{1}{2\mu_0}\left(\frac{\partial A}{\partial z}\right)^2 + P(A) = P_{tot}(x) \tag{1.51}$$

From (1.37), we find that the left-hand side of equation (1.51) is the total pressure (magnetic + thermal), which is now independent of z; and the right-hand side is

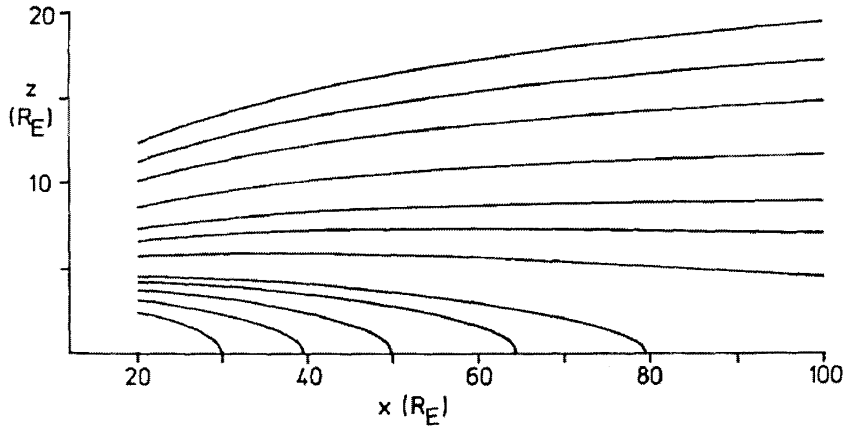

Figure 1.4 : An illustration of the field lines calculated from the integration (1.52). This figure was adopted from Fig. 3 in *Birn et al.* [1975] [7].

an integral constant, which represents the boundary values of the thermal plasma pressure in the neutral sheet. The physical meaning of equation (1.51) is thus a 1D force balance in z direction. This is a result of the tail approximation. Integrating (1.51) once again with respect to A, we obtain a parametric representation of the equilibrated field line

$$z(x, x_0) = \int_{A(x)}^{A(x_0)} \frac{dA}{\sqrt{2\mu_0(P_{tot}(x) - P(A))}} \tag{1.52}$$

in which x_0 is the x coordinate of the neutral sheet crossing point of the field line. An example of the integrated field lines is given in Figure 1.4. Note that, in this theory the functional form $P(A)$ remains a free function, and needs to be specified by other sources. Total pressure $P_{tot}(x)$ is given by other statistical models.

This theory is easily generalized into three dimensions [*Birn*, 1987 [3]]. In this case, Euler potentials (Ref. subsection 1.1.5) are used in stead of the flux function as

in the 2D situation. The 1D force balance in z direction still applies, except that B_y is now present

$$\frac{1}{2\mu_0}(B_x^2 + B_y^2) + P(\alpha, \beta) = P_{tot}(x, y) \tag{1.53}$$

Without loss of generality, *Birn* expressed β as a function of x, y, and α. Hence by the definition of Euler potentials (1.25), B_x and B_y write

$$B_x = -\frac{\partial \alpha}{\partial z}\frac{\partial \beta(x, y, \alpha)}{\partial y} \tag{1.54}$$

$$B_y = +\frac{\partial \alpha}{\partial z}\frac{\partial \beta(x, y, \alpha)}{\partial x} \tag{1.55}$$

Combining (1.54) and (1.55) with (1.53), they derived the 3D counterpart of equation (1.51)

$$\left(\frac{\partial \alpha}{\partial z}\right)^2 |\nabla \beta|_\alpha^2 = 2\mu_0\big(P_{tot}(x, y) - P(\alpha, \beta)\big) \tag{1.56}$$

Following the same algebra as in the 2D case, equation (1.56) can be integrated and the parametric representation of field lines obtained

$$z(x, y) = z_0(x, y) \pm \int_{\alpha_0}^{\alpha} |\nabla \beta|_\alpha \frac{d\alpha}{\sqrt{2\mu_0(P_{tot}(x, y) - P(\alpha, \beta))}} \tag{1.57}$$

where z_0 is the location of the neutral sheet and $\alpha_0(x, y) = \alpha_0(x, y, z_0)$ is the value of α in the neutral sheet.

Compared to the 2D linear Grad-Shafranov model, the 3D asymptotic theory has several advantages. Obviously, it can take into account the y direction. Furthermore, notice that in equation (1.57) the theory did not assume a plane shape of the neutral sheet, hence it is capable of dealing with curved neutral sheet, which might be caused

by the Earth's dipole tilt or the presence of IMF B_y component. *Birn* applied this theory to the study of the flaring of far tail plasma sheet toward the flanks [*Birn*, 1989 [4]] and the distortion of the plasma sheet under influence of cross-tail magnetic field [*Birn*, 1990 [5]], and achieved qualitative agreement with observations. However, although this theory appears analytic, in practice integrations like the one in (1.57) often require tedious numerical quadrature; only under quite special cases are they able to be calculated analytically. We will further discuss this theory in Chapter 3.

1.2.3 The MAG-3D code

Cheng [1995] [12] and *Zaharia and Cheng* [2003b] [39] developed a 3D numerical code that achieved the magnetosphere equilibrium by solving equations (1.29) and(1.30) iteratively. More specifically, using equation (1.12) and (1.25), they expanded equations (1.29) and (1.30) in terms of Euler potentials

$$\vec{J} \cdot \nabla\alpha = \frac{1}{\mu_0}\nabla \cdot \left[(\nabla\alpha)^2\nabla\beta - (\nabla\beta \cdot \nabla\alpha)\nabla\alpha\right] = -\frac{\partial P}{\partial\beta} \tag{1.58}$$

$$\vec{J} \cdot \nabla\beta = \frac{1}{\mu_0}\nabla \cdot \left[(\nabla\beta \cdot \nabla\alpha)\nabla\beta - (\nabla\beta)^2\nabla\alpha\right] = +\frac{\partial P}{\partial\alpha} \tag{1.59}$$

On the first sight, equation (1.58) and (1.59) appear to be coupled 3D equations. However, on constant α surfaces, equation (1.58) reduces to a 2D inhomogeneous elliptic equation of β, with right-hand side being the source term; and on constant β surfaces, equation (1.59) a 2D equation of α. Therefore, they carefully selected their coordinate system so that the constant coordinate surfaces were coincident with the constant α and β surfaces. To solve these equations, they first fix one coordinate

surfaces, for instance the constant α surfaces, and solve equation (1.58) on every α surface to update the β values. After this step, they then fix the newly computed β surfaces, and on these surfaces solve equation (1.59) to update the α values. Iteration is continued until the coordinate surfaces do not change any more, that is, an equilibrium has been reached.

Despite the elegant design of the numerical approach and the good equilibrium it can achieve, the MAG-3D code has several shortcomings. First, the code uses constant α surfaces as inner and outer boundaries, which restrict the code to closed-fleld-line regions. Hence, this code is ideally used in the study of the near Earth equilibrium, but is unable to be applied to calculate the equilibrium between plasma sheet and magnetotail lobes. Second, even for closed-field-line domain, it can not extend too far into the magnetotail. Because for the highly stretched field lines, the large discrepancy between the greatest and smallest field strengths and the strong deformation of the coordinate surfaces will lead to numerical problems in computation [*Zaharia et al.* 2004 [38]]. Third, in the iteration procedure, boundary surfaces are never updated but fixed, thus initial values on boundaries continuously affect the final result. And finally, it is incapable of dealing with the Earth's dipole tilt.

1.2.4 Magneto-frictional relaxation method

In contrast to all the previous methods for obtaining magnetosphere equilibrium, be it analytical or numerical, the magneto-frictional relaxation method [*Hesse and Birn*,

1993 [17]] does not try to solve the Grad-Shafranov equation (1.34), but seeks for the minimum potential energy state of the system by artificially dissipating energy while conforming to the MHD constraints. *Chodura and Schlüter* [1981] [13] have shown that, a minimum of the potential energy implies that the MHD force density $-\nabla P + \vec{J} \times \vec{B}$ vanishes everywhere. Therefore, a minimum potential energy state is also an equilibrium state.

To dissipate energy, *Hesse and Birn* added a viscous term and a frictional term into the MHD momentum equation (1.2), namely

$$\rho \frac{d\vec{v}}{dt} = \vec{J} \times \vec{B} - \nabla P + \nu \nabla^2 \vec{v} - \alpha \rho \vec{v} \tag{1.60}$$

where ν is the viscosity coefficient and α here is the friction coefficient. The minimum potential energy state is approached as the system evolves in the modified MHD world. Mathematically, it can be shown that the rate of change of the total potential energy is expressed by

$$\frac{d}{dt} \int_V dV \left(\frac{B^2}{2\mu_0} + \frac{1}{2} \rho v^2 + \frac{P}{\gamma - 1} \right) = \int_V dV \left(-\alpha \rho v^2 + \nu \vec{v} \cdot \nabla^2 \vec{v} \right) \tag{1.61}$$

In the final relaxed state, the velocity $\vec{v}$ vanishes, and so does the dissipation.

It should be mentioned that, although such evolution process may never happen in nature, the actual form of the energy dissipation terms is nonetheless unimportant, provided that they vanish in an equilibrium state, since the final lowest potential energy state does not depend on the evolutional path the system actually takes (except for the different choices of γ value) [*Hesse and Birn*, 1993 [17]]. Therefore, we are

free to pick from many options the most efficient dissipation mechanism, no matter if it is viscous or frictional.

The friction code we are going to discuss in this dissertation is based on this work.

Chapter 2

The Tilted-Dipole Magneto-Friction Code

This chapter describes the infrastructure and algorithms of the new version of the friction code. The friction code uses a 3D stretched Cartesian grid. All data, including density, pressure, velocities and magnetic field, are stored on grid nodes. The friction code algorithm is roughly as follows: initial magnetic field and pressure profile are set either from observation-based statistical models or from the calculation result of other coupled numerical applications, such as the Rice Convection Model (RCM). Among statistical magnetic field models, Tsyganenko models [for example, *Tsyganenko*, 1989 (T89) [26], *Tsyganenko and Stern*, 1996 (T96) [28]] are the most widely used; for pressure model, the options could be Spence-Kivelson model [*Spence et al.*, 1989 [25]] or Tsyganenko-Mukai model [*Tsyganenko and Mukai*, 2003 (TM03) [27]]. However, although magnetic field models provide 3D magnetic field, pressure models usually only give 2D pressure distribution in the neutral sheet. 3D pressure distribution is obtained by assuming that initial pressure is constant along field lines, which is a feature of equilibrium (Ref. subsection 1.1.3). After the initial setup, the system is evolved in "time" by integrating the modified MHD equations with additional viscous and frictional terms (Ref. subsection 1.2.4). Time in the friction code is unphysical, because the relaxation procedure does not really happen in nature. The system is continuously relaxed until the pre-designated number of iterations are finished, or a

minimal force-imbalace criterion is met.

Section 2.1 introduces the algorithm for tracing magnetic field lines in the friction code. Field line tracer constitutes a fundamental part of the friction code, and it is repeatedly called during the initial setup, locating the position of the neutral sheet and computing the flux tube volume. Section 2.2 addresses the issues of generating a stretched Cartesian grid for the computational domain, the classification of different magnetic field regions according to the field line topologies, and the initial 3D pressure distribution. Section 2.3 describes the boundary conditions. Section 2.4 gives a brief description on the normalization of MHD equations and the third order Adams-Bashforth algorithm used to solve the equations. Subsequently, an assessment of the quality of the equilibrium is discussed in this section. And in section 2.5, the PV^{γ} correction algorithm is described.

2.1 Magnetic field line tracer

2.1.1 Numerical methods

The magnetic field line tracer in the friction code has three functions: positioning space path of a field line, calculating the flux tube volume of a field line, and locating its neutral sheet crossing point and ionospheric footprints. The problem of tracing a magnetic field line in a known magnetic field can be viewed as solving the following first order ordinary differential equation (ODE)

$$\frac{d\vec{x}}{ds} = \hat{b}(\vec{x}) \tag{2.1}$$

with the initial condition a given starting point, where s is the field line arc length and $\hat{b}$ is the unit vector of the local field direction. Standard algorithms for solving ODE's are also applicable for tracing field lines. The field line tracer used by the friction code has two options: the adaptive Euler method and the adaptive forth order Runge-Kutta method.

In practice, tracing field lines can be far more challenging than it looks. First, to integrate equation (2.1), we need to know the functional form of its right-hand side. Indeed, Tsyganenko models provide analytical forms of $\vec{B}(\vec{x})$, but using Tsyganenko models directly in tracing can be computationally expensive. A typical friction code run has the grid size of roughly 100 by 100 by 100 in each Cartesian coordinate, that amounts to a total of 1 million grid points. Each grid node requires a field line tracing to determine on which field line it resides, and where the field line crosses the neutral sheet in order to setup initial pressure. Typically, tracing one field line under the current error tolerance in the friction code needs the order of 1000 integrating steps. Consequently, the initial setup would have to call Tsyganenko model at least 10^9 times as using it directly (not even counting for the trial steps in adaptive method), and that is extremely time consuming (several days using the current computational power at Rice). Moreover, if the initial magnetic field is set up using the result of other computations, their magnetic field data are usually stored at grid nodes. Therefore, it is a reasonable choice to first set the magnetic field on the friction code grid, and then obtain the field data at any space position by interpolation of the data stored

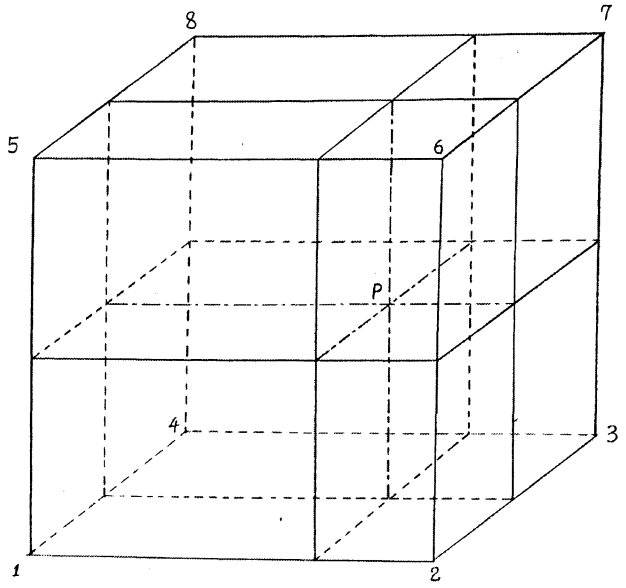

Figure 2.1 : A grid cell illustrating the linear interpolation. Point P is the space position of interest. Vertices 1, ..., 8 are the nearest 8 grid nodes surrounding P.

on the nearest neighboring grid nodes.

The 3D interpolation algorithm used in the friction code is a simple linear interpolation involving the nearest 8 grid nodes that constitute the vertices of a cubic enveloping the space point of interest, as illustrated in Figure 2.1. The interpolated value at point P is a weighted average over the values of the 8 neighboring grid nodes. The weight, for grid node 1 in Figure 2.1 as an example, is the ratio between the volume of the small cubic, which has node 7 and point P as two opposite vertices, and the total volume of the big grid cell. While this interpolation algorithm works fine for scalars, it is only approximately accurate for the magnetic field. Linear interpolation does not preserve the divergence-free property of the interpolated field. In most regions in the magnetosphere, that accuracy is good enough; but near the null

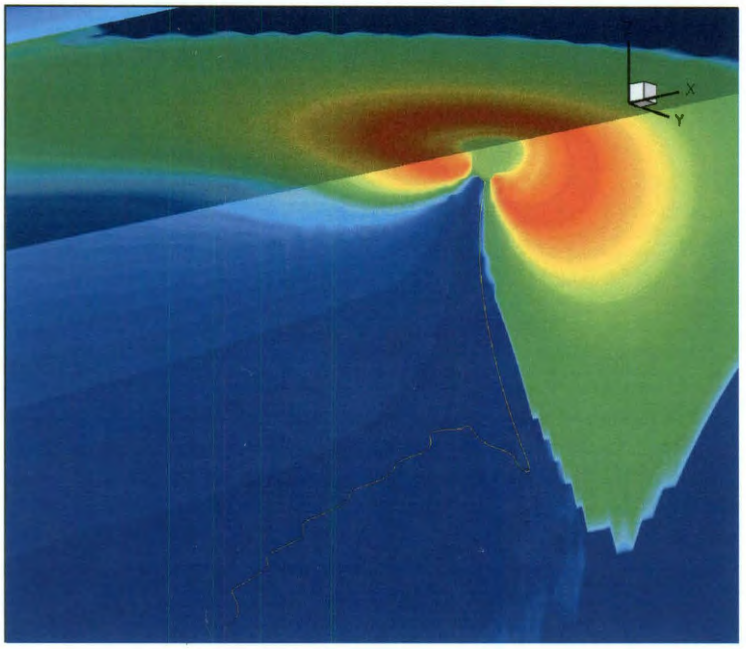

Figure 2.2 : An example of the meandering magnetic field line tracing caused by the linear interpolation. This field line (yellow) has one end in the southern ionosphere and threads through the dawn-side magnetopause. Color map in the background shows the pressure distribution around the Earth. Magnetic field model is T96, with parameters 30° tilt angle, 1.5 nPa solar wind dynamic pressure, $Dst = -20$, IMF $B_y = 4.0$ nT, $B_z = -4.0$ nT. Tracing method is adaptive Euler.

point where magnetic field is very weak and changes sharply in a small region, the interpolated magnetic field will cause the tracer to either meander or even be trapped around some point forever, see Figure 2.2. Yet divergence-free interpolation often requires far more complicated algorithms, or storing data at the center of each grid cell face. Since interpolation is the most frequently called routine in the friction code, complicated and slow algorithms are not feasible. This is a compromise in the current version of the friction code.

Secondly, the tracing of a field line does not only demand a precise positioning

of its path in space, but equally importantly, a precise integration of its flux tube volume (1.17). The contribution to the flux tube volume integration mainly comes from the portion of the field line where magnetic field strength is the weakest. The same spatial error tolerance will introduce a much larger error in flux tube volume when the field is weak. Therefore, in addition to the three spatial ODE's in (2.1), the tracer incorporates a fourth ODE to consecutively calculate the integration of flux tube volume

$$\frac{d\tau}{ds} = \frac{1}{B(\vec{x})} \tag{2.2}$$

where τ denotes for the flux tube volume. When estimating the precision of each tracing step, we employ two error tolerances: one is for spatial error and the other for error in the flux tube volume. Each one of these two errors can dominate in certain regions: when tracing near to the Earth, precise positioning of the ionosphere footprint is important whereas flux tube volume integration is unimportant, the spatial error dominates; far in the tail, the calculation of flux tube volume is critical and space positioning is not the major concern, the flux tube volume error dominates; if the field line goes out of the magnetopause, since flux tube volume is no longer meaningful, both errors are relatively unimportant, because we only care about on which boundary the tracing ends (Ref. subsection 2.2.2). The friction code has a carefully designed error estimation mechanism that automatically restricts or relaxes either or both of the two error tolerances. Only when both the two errors are below the designated error tolerances does the adaptive tracer advance to the next step,

otherwise, it reduces the current step size and has another trial.

2.1.2 Locating the neutral sheet

The neutral sheet is defined as the sheet in the plasma sheet where the Earthward-tailward polarity of magnetic field vanishes, or equivalently in most cases where the magnetic strength is the weakest for a specific field line. In the zero dipole tilt and zero IMF B_y case, the neutral sheet coincides with the GSM xy plane because of north-south symmetry, hence is known in advance; however in more general cases, the neutral sheet becomes a curved surface determined by the particular magnetic field. Physical quantity values in the neutral sheet are usually of special interests because unique physics often happens there, for example, the cross-tail current density concentrates near the neutral sheet, and chaotic motions of particles trapped by the magnetic field often occur in the neutral sheet, which casts their adiabatic invariance violated. Thus, locating the neutral sheet is another function of the field line tracer.

The neutral sheet crossing criterion is adopted from *Tsyganenko and Mukai* [2003] [27]: the local position of the neutral sheet is at the place where the GSM radial component of the magnetic field

$$B_\rho = B_x \cos\phi + B_y \sin\phi \tag{2.3}$$

reverses its sign, where ϕ is the GSM longitude angle. Note, in the magnetotail the neutral sheet position as defined by *Tsyganenko and Mukai* is usually the same as the weakest strength point along a field line, but close to the Earth when there is dipole

tilt, they are not identical. However, the difference between these two definitions is unimportant, because on the one hand it is small, and on the other hand near to the Earth the concept of neutral sheet itself is not meaningful. The reason we adopt *Tsyganenko and Mukai*'s definition is that it is also applicable independent of field line tracings. In many situations during a friction code run, it is often required to know the neutral sheet position without the knowledge of every field line. Thus, for the consistency of the code, the field line tracer uses this definition also.

In practice, there are a few issues that we need to pay attention to. First, a field line may have multiple B_ρ sign reversals, for example in the case of a flux rope. For this case the reversal of the smallest field strength is designated as the neutral sheet crossing point. Second, B_ρ does not only reverse its sign in the neutral sheet, but also in the polar cusps and maybe on the magnetopause. In the friction code, these locations are ruled out by only looking for the neutral sheet outside of the spatial region confined by a 3D doubly infinite cone, as shown in Figure 2.3 , which has its apex at the GSM origin, axis tilted $\theta/2$ in the same sense as the dipole tilt (θ is the tilt angle), and half aperture $\frac{1}{2}(\pi - \theta) - \delta$, where δ is a small angle to prevent the cone from touching the neutral sheet. The cone method works as long as the tilt angle is not too close to 90°, and its validity is proved by trial and error. Figure 2.4 gives an example of the neutral sheet determined by the *Tsyganenko and Mukai* definition.

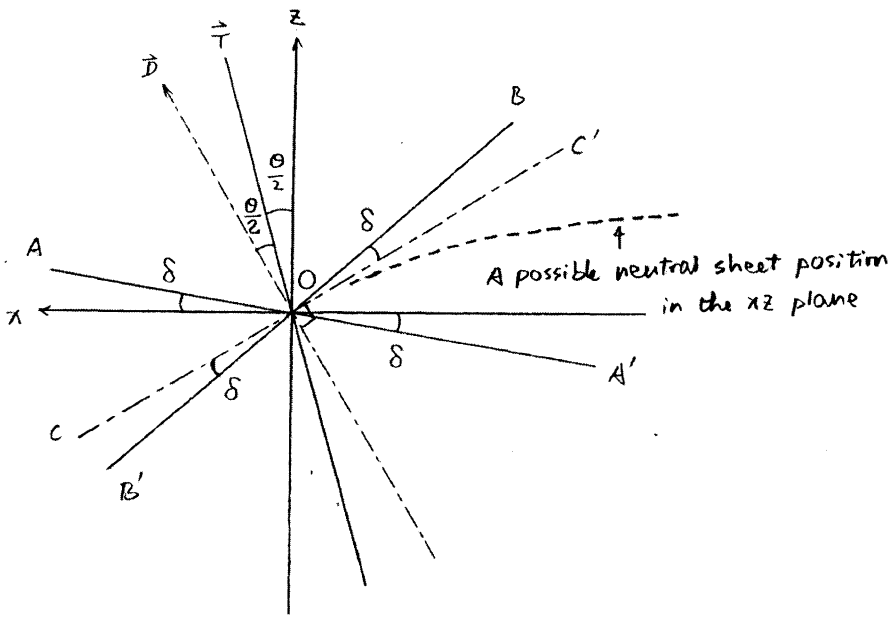

Figure 2.3 : A geometrical illustration of the cone in the GSM xz plane. The Earth is located at the origin point O. Earth's dipole axis is $\vec{D}$, and has tilt angle θ. Straight line COC' is perpendicular to $\vec{D}$. $\vec{T}$ is the axis of the cone, which has the angle $\theta/2$ between the GSM z axis. Straight lines AOA' and BOB' are two generatrices of the cone. The angle δ is shown in the figure. The 3D cone is generated from rotating straight lines AOA' and BOB' around the axis $\vec{T}$.

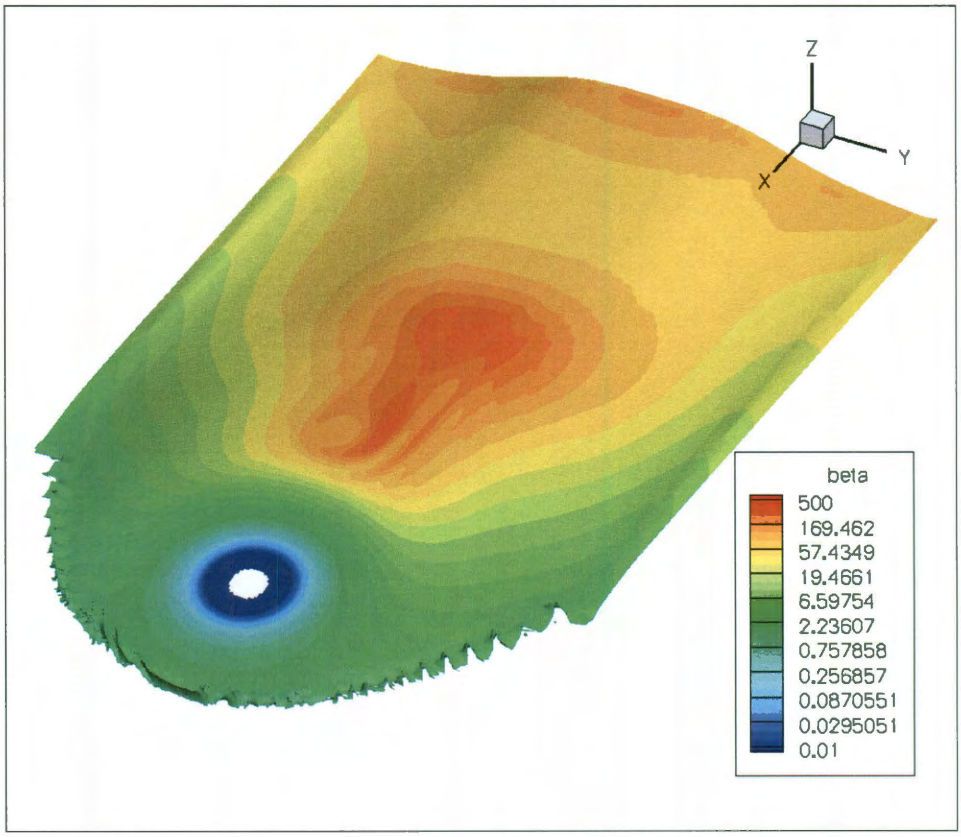

Figure 2.4 : The curved neutral sheet from a friction code result. Initial setup of the code uses Spence-Kivelson pressure model with $Kp = 6$ and T96 magnetic field model with tilt angle 20°, solar wind dynamic pressure 5.0 nPa, Dst -20, AE 0.0, IMF B_y -7 nT and B_z -7 nT. The blank hole is the place of the Earth. The ragged margin on the dayside is caused by the magnetopause. The color map flooded on the neutral sheet is the plasma β value, which is defined as $\beta = \frac{P}{2\mu_0 B^2}$. Note the region of maximum β, it appears at about -25 R_E in the tail.

2.1.3 Accuracy of field line tracing

This subsection gives a comparison of the tracing accuracy between the adaptive Euler and the adaptive Runge-Kutta methods. The precision of field line tracing can be assessed by the departure of its actual ionosphere footprint from the theoretical footprint. In one test, we start the tracer from one ionosphere in a dipole field, and see how far it is from the conjugate footprint in the other ionosphere, see Table 2.1. In a second test using a realistic friction code result, we start the tracer from the northern ionosphere till it reaches the southern one, and then send it back exactly from the southern footprint and see if it results in identical field lines. The results are shown in Figure 2.5 and Figure 2.6.

In Table 2.1, the coordinates of start and end points are given in pairs of colatitude and longitude, the radius of "ionosphere" is 3 R_E. "NSC" stands for "Neutral Sheet Crossing", and their coordinates are given in a Cartesian frame with unit R_E. "FTV" stands for "Flux Tube Volume", with unit R_E/nT. It is seen that both methods yield accurate tracings. The most notable difference is adaptive Runge-Kutta method used significantly fewer steps than adaptive Euler method used, or in other words, adaptive Runge-Kutta method took larger step sizes. But this does not mean that adaptive Runge-Kutta method is more computationally efficient. In fact, it is slower than adaptive Euler method because Runge-Kutta method requires four samples of the magnetic field at each step to evaluate the right-hand side of Equation (2.1), whereas Euler method only needs one. In addition, from the neutral sheet crossings and flux

Table 2.1 : List of tracing test results in dipole field.

Method	Start	End	NSC	FTV	Steps
Theory	(15.0, 180.0)	(165.0, 180.0)	(−44.7846, 0.0, 0.0)	1.2029E2	
	(45.0, 180.0)	(135.0, 180.0)	(−6.0, 0.0, 0.0)	3.7895E-2	
	(60.0, 180.0)	(120.0, 180.0)	(−4.0, 0.0, 0.0)	6.5751E-3	
Adaptive	(15.0, 180.0)	(165.0006, 180.0000)	(−44.7880, 0.0, 0.0)	1.2034E2	3081
Euler	(45.0, 180.0)	(134.9999, 180.0000)	(−6.0002, 0.0, 0.0)	3.7901E-2	348
	(60.0, 180.0)	(119.9998, 180.0000)	(−4.0000, 0.0, 0.0)	6.5752E-3	358
Adaptive	(15.0, 180.0)	(164.9990, 180.0000)	(−44.7846, 0.0, 0.0)	1.2029E2	1181
Runge-	(45.0, 180.0)	(134.9929, 180.0000)	(−6.0000, 0.0, 0.0)	3.7894E-2	107
Kutta	(60.0, 180.0)	(119.9877, 180.0000)	(−3.9999, 0.0, 0.0)	6.5746E-3	47

tube volumes, it is evident that Euler method is always overshooting. In this tracing test, the adaptive Runge-Kutta method seemingly yields slightly more accurate result than the adaptive Euler method, but in realistic applications, the magnetic field is much more complicated than the dipole field, and the comparison might be different.

In the test against a realistic friction code magnetic field with a flux rope in the tail, shown in Figure 2.5 and 2.6, identical forth and back field line tracings were obtained for both methods, as long as the tracer did not wade into the flux rope, even if the field line was highly stretched as the one to the far right. However, when the tracer threads through the flux rope, neither method could return satisfactory result, because the field strength was extremely weak there ($\sim$ 1 nT).

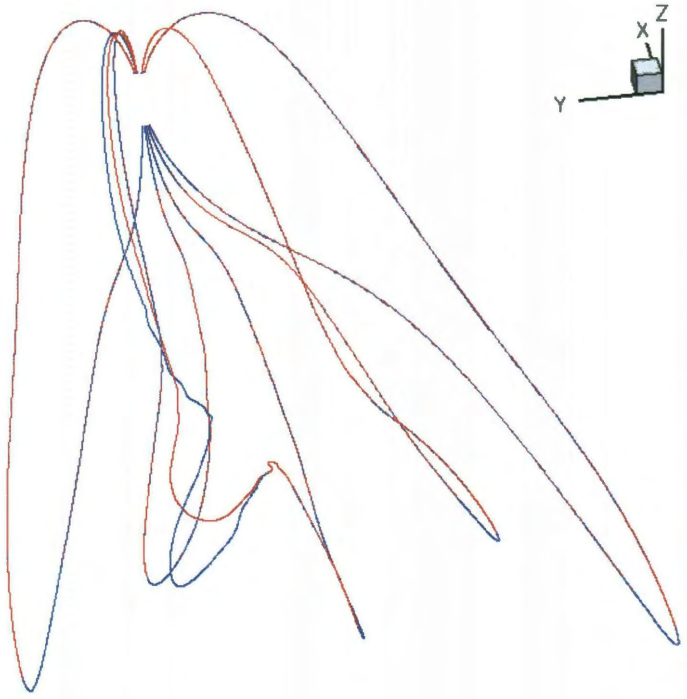

Figure 2.5 : Tracing test of adaptive Euler method in a friction code magnetic field with highly stretched magnetotail. The tracer starts from five different points in the northern ionosphere, and follows along the red field lines to the southern ionosphere, and then returns along blue field lines. Four out of these five tracings have virtually identical field lines except the central one, which threads through a plasmoid generated by the friction code.

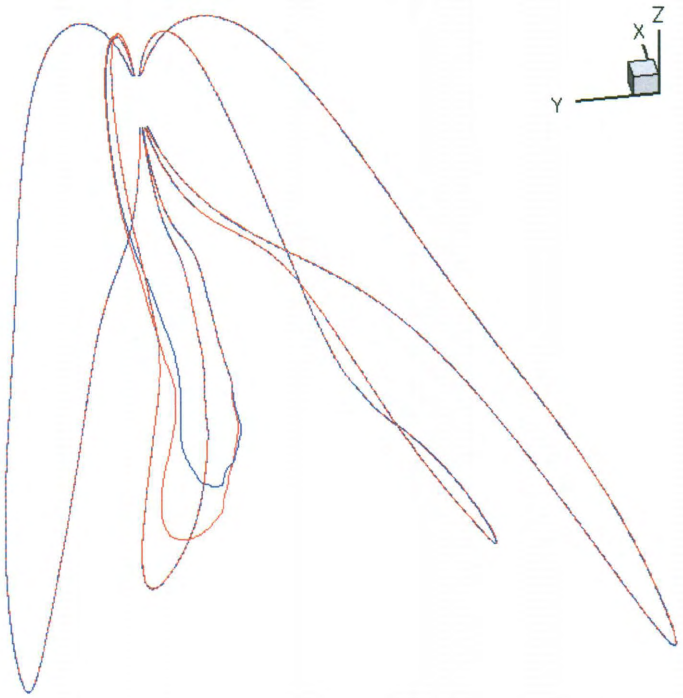

Figure 2.6 : Tracing test of adaptive Runge-Kutta method in the same magnetic field as in Figure 2.5 under the same conditions. For the four good tracings in Figure 2.5, adaptive Runge-Kutta method gives the same result; for the bad one in Figure 2.5, adaptive Runge-Kutta method also gives a bad but different result.

2.2 Initial setup

2.2.1 Grid generation

In this version of the friction code, the numerical grid is generated separately. To increase computational accuracy, the Cartesian grid is stretched such that grid nodes concentrate around the Earth and near the plasma sheet, as illustrated in Figure 2.7. The stretched grid is generated by the use of grid density functions. Along each

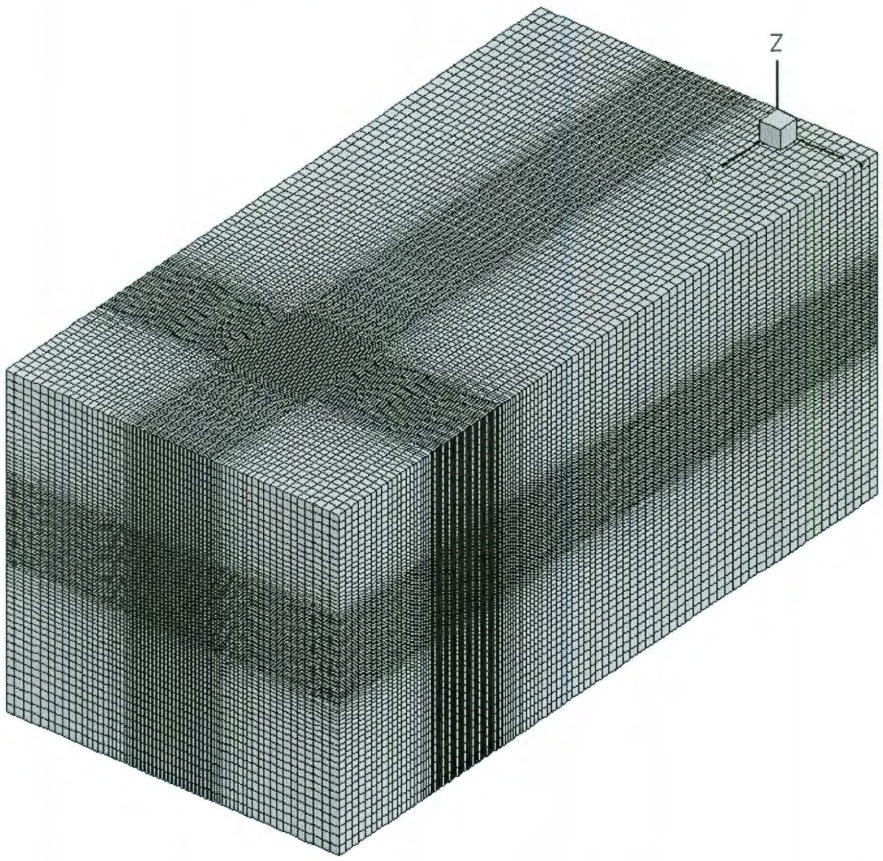

Figure 2.7 : An example of the stretched Cartesian grid in the friction code. Grid nodes concentrate around the Earth and near the plasma sheet. Note, in z direction, the fine region is not centered at $z = 0$ plane but shifted upward to cover the plasma sheet when dipole tilt is positive.

dimension of the grid, there is a grid density function specifies the functional relation of the grid density, or the inverse of grid space, with the coordinates. In the fine region of the grid, grid density is high and constant; in the coarse region, grid density is low and constant; and between these two regions, grid density transitions linearly. The integration of the grid density function over coordinate then gives the positions of every grid tick mark in that dimension. Note that, although the grid density function is not smooth, its integration is, thus there is no abrupt change in grid spacing from one region to another. In practical use of this grid generator, the user has the freedom to designate the position and the size of the fine and the coarse region, and the size of the transitioning region (hence how fast the grid density transitions), and the grid spaces in the fine and coarse regions respectively.

2.2.2 Magnetic field regions

During its initial setup, the friction code has a function that can classify the entire computational domain into five kinds of "magnetic field regions" according to their different magnetic field topologies. Because of the frozen-in flux condition in ideal MHD, magnetic field topology never changes during the convection (Ref. subsection 1.1.2). Therefore, knowing the magnetic field topologies of the domain will give us great advantages in computation and save a lot of effort. For example, the option of PV^{γ} correction (refer to subsection 2.5) is only performed for closed field lines, without the knowledge of field topologies in advance, we would have to try field line

tracings for every single grid node in the domain during the PV^{γ} correction; but with such knowledge, we are able to preselect those grid nodes lying on closed field lines even before the PV^{γ} correction begins.

The five magnetic field regions are classified as: 1) inside the Earth; 2) closed field line region which is on closed field lines that have both of their ends in the ionosphere; 3) tail lobe region which is on tail lobe field lines that have one of their ends in the ionosphere, and the field lines extend into the magnetotail; 4) open field line region which is on open field lines that have one of their ends in the ionosphere and the other connected to the IMF; and 5) IMF region which is on the interplanetary field lines.

The classification of magnetic field regions is determined by field line tracing during the initial setup. To know exactly where the field line tracer goes, we often need to trace out of the computational domain. Therefore, during the setup of the friction code, it has two nested domains, as shown in Figure 2.8. The larger domain B incorporates the entire magnetopause except for the intersection on the GSM x minimum face. Consequently, all closed field lines will never encounter any boundary of domain B during their tracing. In contrast, IMF field lines will have both their ends lying on the boundaries of domain B. If the x dimension of domain B is long enough, we regard all the field lines that have one end on the Earth and the other intersecting with the x minimum face of domain B as tail lobe field lines, and those have one end on the Earth and the other end intersecting other faces of domain B

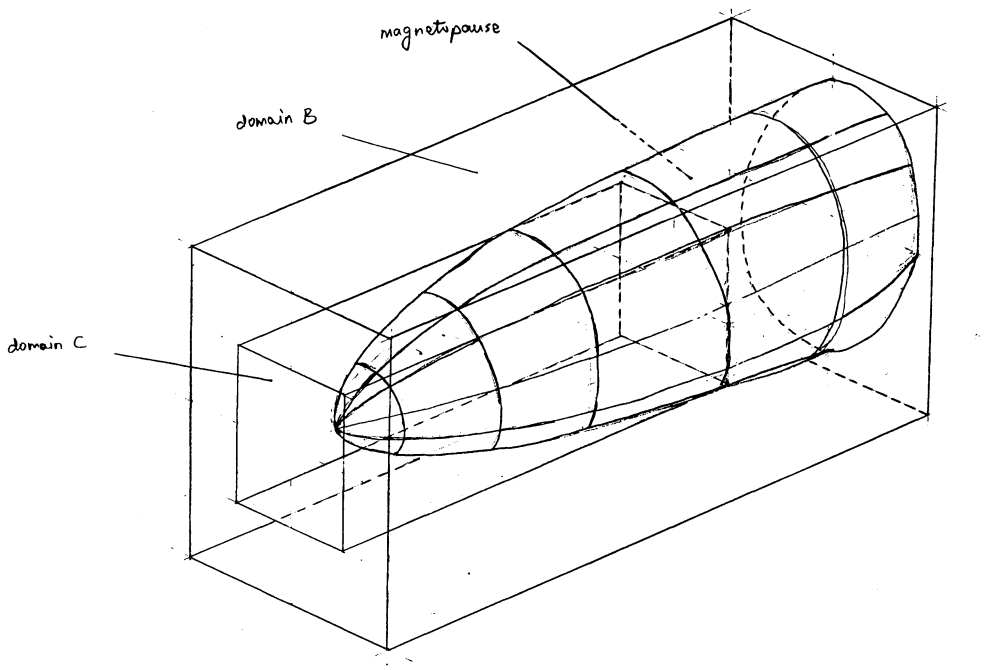

Figure 2.8 : Illustration of the two nested domains used to classify the magnetic field regions. The smaller box, domain C, is the computational domain. The bigger box, domain B, is the domain for field line tracings. Domain B shall be large enough to incorporate the entire magnetopause except the intersection on the GSM x minimum face. In the case of open magnetopause, domain B shall also be long enough in order to let the open field lines intersect on faces other than the GSM x minimum face, to distinguish them from tail lobe field lines.

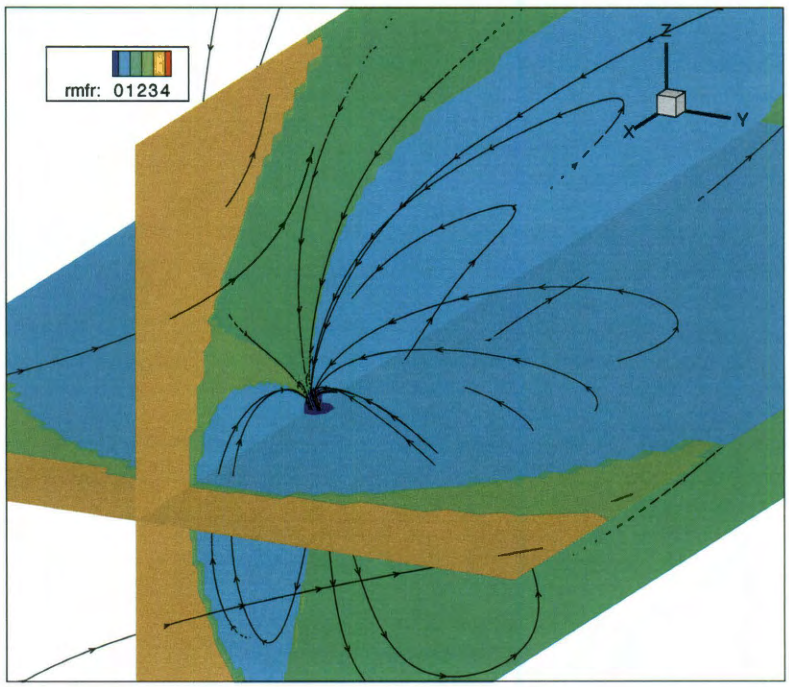

Figure 2.9 : The magnetic field regions of the computational domain in an example friction code run. Magnetic field is from T96 model. The "rmfr" value 0 corresponds to the 1st kind of magnetic field regions, and 4 corresponds to the 5th kind.

as open field lines. The longer domain B is, the more accurate this method will be. During the initial setup, for every grid node in domain C, the magnetic field line through it is traced, and then that grid node is classified into one of the five magnetic field regions according to the topology of the field line it resides on. Figure 2.9 gives an example of the magnetic field regions.

A convenient byproduct of this classification is that the friction code knows where the magnetopause and the polar cusps are, no matter whether the magnetic field model provides such information (for instance, T89 does not give the magnetopause position). With this knowledge, we are able to avoid trying to find an equilibrium in

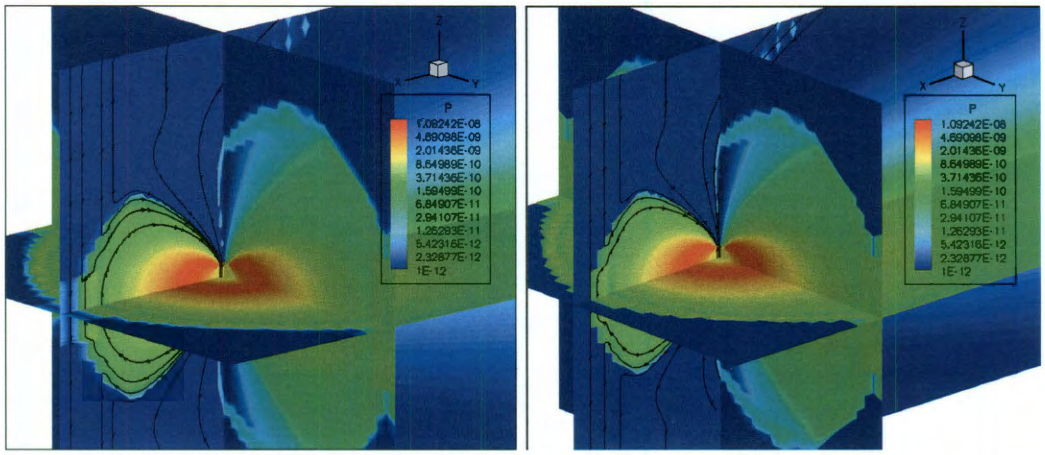

(a) Without high density magnetosheath (b) With high density magnetosheath

Figure 2.10 : These are two friction code results with identical initial setup, except for the use of high density plasma in the magnetosheath. In the left panel, dayside plasma protrudes out into the magnetosheath whereas in the right panel it is kept sharply within the magnetopause. These simulations used T96 magnetic field model with IMF $B_z = -5$ nT. Note the open field lines in the polar cusps. Colors represent plasma pressure.

regions where it is not possible to find an equilibrium and are not of physical relevance, such as the magnetosheath and the magnetopause, by filling them with extremely high density and relatively low pressure (and hence extremely low temperature) plasma. This makes the "temporal" evolution of plasma in those regions very slow so that the effect of their existence could be minimized. Also, the high density plasma prevents the relatively hot and dilute plasma inside the magnetopause from flowing out of the magnetopause or crossing the polar cusp from the dayside into the nightside tail lobes. Figure 2.10 shows a comparison between these two scenarios. As a side discussion, density ρ in the friction code is arbitrary because the final equilibrium does not depend on it [*Lemon et al.*, 2003 [22]].

2.2.3 Setup of initial pressure

Because statistical pressure models only provide 2D pressure distribution in the neutral sheet, the 3D initial pressure is populated by mapping the 2D distribution along field lines. For grid nodes in the closed field line region, their pressure is set as the 2D pressure at their field lines' neutral sheet crossing points. For grid nodes in the tail lobes, their field lines do not cross the neutral sheet but intersect with the GSM x minimum face of domain B (in Figure 2.8). Thus, an initial pressure distribution on this face is required.

The initial pressure distribution on the back face of domain B is obtained by integration of equation (1.11). From (1.11) and 1.12, we eliminate $\vec{J}$ and obtain

$$\nabla(P + \frac{B^2}{2\mu_0}) = \frac{1}{\mu_0}(\vec{B} \cdot \nabla)\vec{B} \tag{2.4}$$

Integrating equation (2.4) along z direction, starting from the neutral sheet, we have

$$(P + \frac{B^2}{2\mu_0})\Big|_z = \frac{1}{\mu_0}\int_{z_0}^{z}(\vec{B} \cdot \nabla)B_z\, dz + (P + \frac{B^2}{2\mu_0})\Big|_{z_0} \tag{2.5}$$

in which z_0 denotes for the position of the neutral sheet. With the known 3D magnetic field, we could thus divide the back face of domain B into a dense xz mesh, then find the neutral sheet positions on this mesh, and evaluate the integration in (2.5) along every vertical line to have a pressure distribution on the mesh. Pressure at the footprint of a tail lobe field line on the back face is then referenced from the mesh using the linear interpolation introduced in subsection 2.1.1. Occasionally, integration (2.5) may give negative thermal pressure values far from the neutral sheet. This reflects an

inconsistency between the statistical magnetic field model and the statistical pressure model. In these cases, a uniform ΔP is added to the entire magnetosphere to eliminate the negative pressure. Since the gradient of a constant function is zero, this additional ΔP does not affect the final equilibrium.

Pressure for a grid node in the magnetosheath is set uniformly by the lowest pressure in the tail lobes, in order to minimize their influence.

2.3 Boundary conditions

The boundary conditions for the computational domain are rigid wall for the fluid and perfect conductor for the magnetic field. Specifically, they read $\frac{\partial}{\partial n}[\rho, P, \vec{B}_t] = 0, \vec{v} = 0$ at the boundaries, and B_n is adjusted to keep the divergence of $\vec{B}$ is zero at boundaries, where subscripts n and t denote for "normal" and "tangential" respectively. Energy flux in ideal MHD is expressed

$$\vec{S} = (\frac{1}{2}\rho v^2 + \frac{\gamma P}{\gamma - 1})\vec{v} + \frac{1}{\mu_0}\vec{E} \times \vec{B} \tag{2.6}$$

The first term is the kinetic energy flux and the second Poynting vector. Eliminating $\vec{E}$ in (2.6) by Ohm's law for perfect conductance, we have

$$\vec{S} = (\frac{1}{2}\rho v^2 + \frac{\gamma P}{\gamma - 1})\vec{v} + \frac{1}{\mu_0}\left(B^2\vec{v} - (\vec{v}\cdot\vec{B})\vec{B}\right) \tag{2.7}$$

It is easily seen from (2.7) that, conservation of kinetic energy of the system only requires the normal velocities to be zero, conservation of electromagnetic energy however requires the total velocities being zero at the boundaries.

A side effect of this energy-conserving perfect conductor boundary condition is, since magnetic field lines are frozen-in the plasma, footprints of field lines at the boundaries cannot move during the relaxation procedure. But as the system evolves, the position of the neutral sheet generally moves, especially when there is finite dipole tilt. Consequently, the shape of the neutral sheet deforms near the boundaries. And this fact suggests us not to put the boundaries too close to the regions we care about most. An example of the neutral sheet deformation is shown in Figure 2.11.

In numerical implementation, first derivatives at the boundaries are calculated by the use of ghost cells. For the boundary condition of $\vec{v}$, in addition to the boundary value 0, its values at the ghost cells are set anti-symmetrically (oppositely) as the values at the corresponding interior cells. This is for the purpose of conserving kinetic energy [*Denton and Hu*, 2009 [14]], but seems to reiterate the homogeneous Dirichlet boundary condition. *Wolf and Sazykin* [see Appendix A] questioned whether it is an over restriction of the boundary conditions by specifying both the 0 boundary values and the anti-symmetric ghost cell values. They suggested that the use of anti-symmetric ghost cell values would imply a Dirichlet boundary condition. Numerical tests of their suggestion revealed that, although macroscopically stable, without specifying the 0 boundary value, grid scale ripples developed near the boundaries, as portrayed in Figure 2.12 as in contrary to Figure 2.13. The reason for this grid scale noise is still unclear.

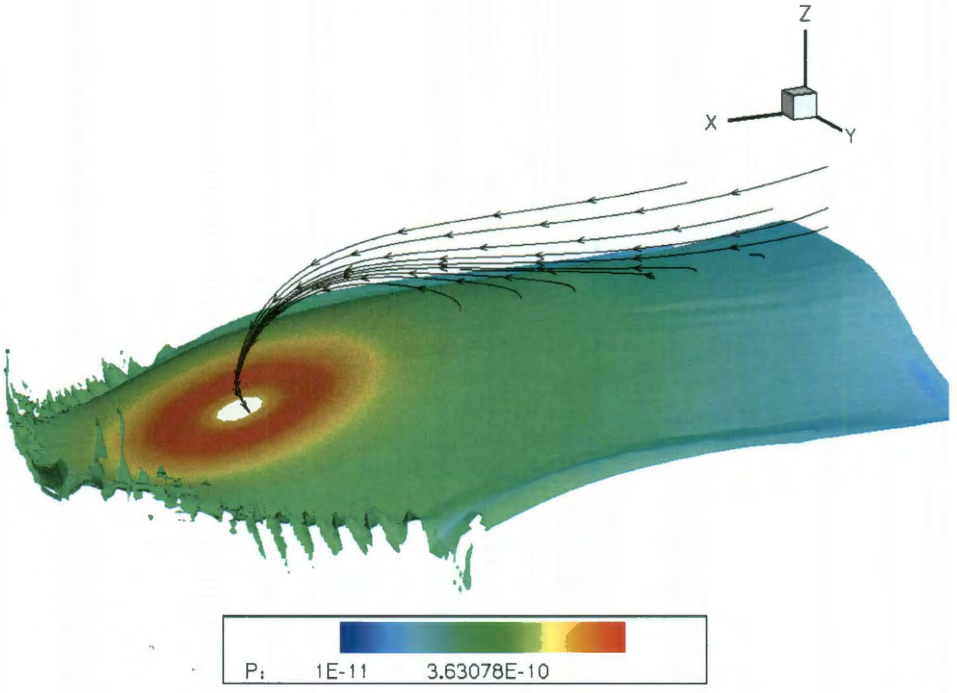

Figure 2.11 : Bent neutral sheet shape caused by the too near tail boundary at -30 R_E. The neutral sheet position at the boundary was fixed, but inside the domain it lowered during the relaxation, thus caused this bent-up shape near the boundary. Magnetic field model is T96 with Earth dipole tilt 30°. Neutral sheet is colored by pressure.

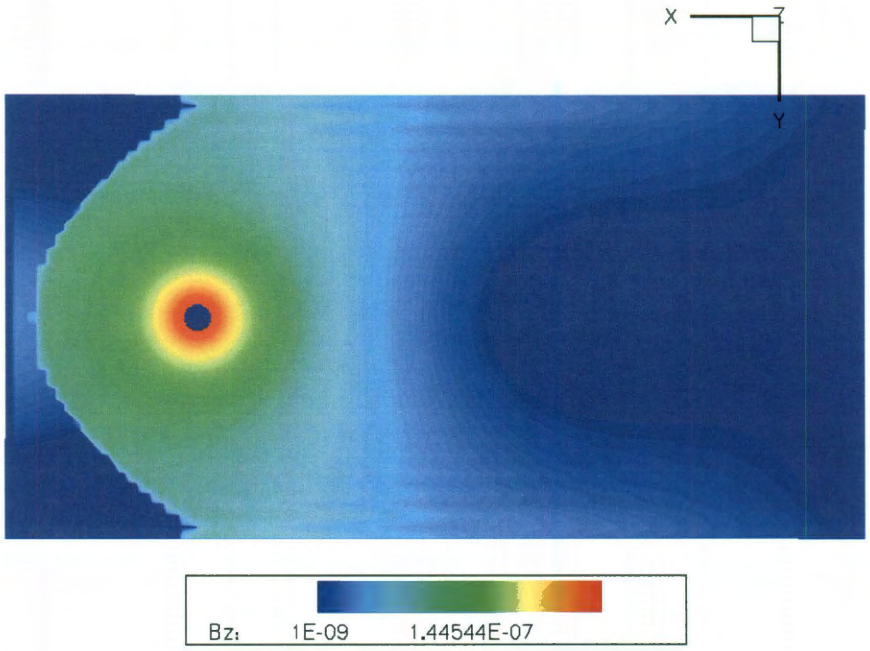

Figure 2.12 : Illustration of grid scale ripples of B_z in the neutral sheet near the boundaries caused by not specifying explicitly $\vec{v} = 0$ at the boundaries.

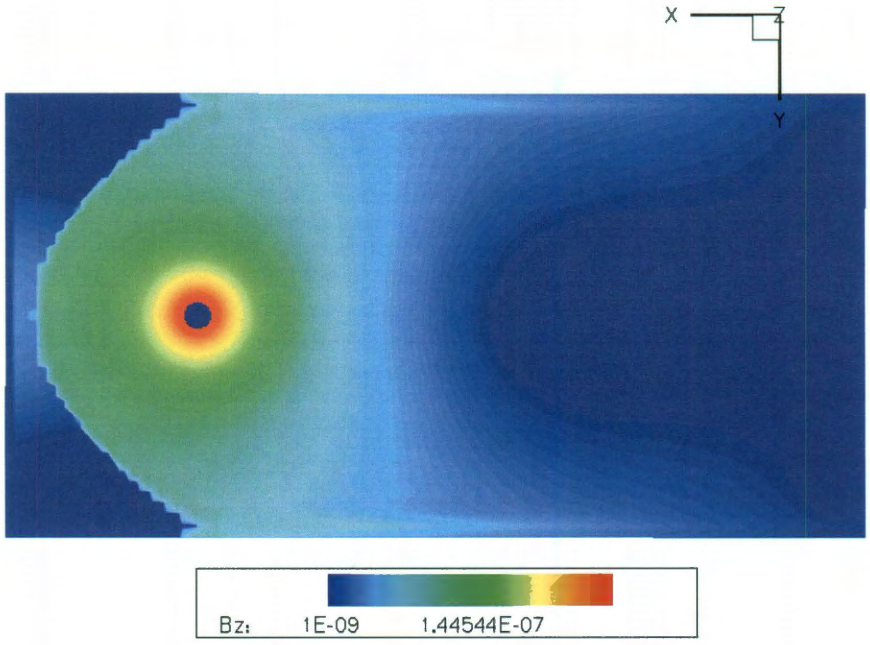

Figure 2.13 : The same plot as in Figure 2.12. The only difference between these two runs is this one specifies the $\vec{v} = 0$ boundary condition explicitly.

2.4 Solving equations and assessment of the equlibrium

Solving the modified MHD equations in the friction code is not a part of the work done for this dissertation, but for completeness, it is presented in this section. Numerical solution of differential equations always starts with converting all physical variables into dimensionless quantities by normalizing them to their characteristic values. In the friction code, the magnetic field is normalized by its typical lobe field strength at $x = -10$ R_E, which is 81 nT; velocity is normalized by the typical Alfvén speed 1000 km/s; and distance is scaled by the radius of the Earth 6380 km [*Hesse and Birn*, 1993 [17]]. From these three basic normalization factors, we are able to derive normalization factors for the other quantities. They are

$$P_0 = \frac{1}{\mu_0} B_0^2 = 5.22 \text{ nPa} \tag{2.8}$$

$$\rho_0 = \frac{P_0}{v_A^2} = 5.22 \times 10^{-21} \text{ kg/m}^3 = 3.13 \text{ protons/cc} \tag{2.9}$$

$$t_0 = \frac{x_0}{v_A} = 6.38 \text{ s} \tag{2.10}$$

in which subscript 0 denotes for the characteristic value, and v_A for Alfvén speed. With these normalization, the fast mode wave speed (1.9) is expressed as

$$v_F^2 = \frac{(B' \cdot B_0)^2/\mu_0 + \gamma(P' \cdot P_0)}{\rho' \cdot \rho_0} \tag{2.11}$$

$$= \frac{B'^2 + \gamma P'}{\rho'} \tag{2.12}$$

where primed values are the values after normalization. In the friction code, initial plasma density is chosen by making v_F to be constant throughout the computational domain.

The numerical algorithm for integrating the equations is the third order Adams-Bashforth method (AB3) [*Canuto et al.*, 1988 [9], and *Lemon et al.*, 2003 [22]]. Compared with other numerical methods for solving advection problems, such as the leap-frog method and Lax-Wendroff method, the AB3 method has the advantage that it remains robust and stable when taking larger time steps. The drawback of AB3 is grid decoupling, which requires the use of a smoother in the code in order to avoid grid scale oscillations of the velocity.

Force imbalance of the system is measured by the acceleration parameter N as

$$N = \int \frac{|\vec{J} \times \vec{B} - \nabla P| \, d^3x}{\rho} \tag{2.13}$$

A typical force relaxation curve is shown in Figure 2.14. In this result, force imbalance is quickly relaxed during the first 400 time steps. Note that, at the end of the friction code run, the system is not completely relaxed, but force imbalance remains a little less than 1/10 of its initial value. This is a character of the friction code. The reason for this residual force imbalance might be the numerical error caused by the finite number of grid nodes.

The friction coefficient α in equation (1.61) determines the rate of relaxation. A high level of α, although seemingly leading to a larger rate of energy dissipation, also reduces the magnitude of $\rho\vec{v}$ by equation (1.60), and thus though the nonlinearity of the dissipation term in (1.61), effectively leads to a lower dissipation rate [*Hesse and Birn*, 1993 [17]]. A too small α on the other hand dampens the system too weakly thereby causing computation time to be wasted on global oscillations. In the friction

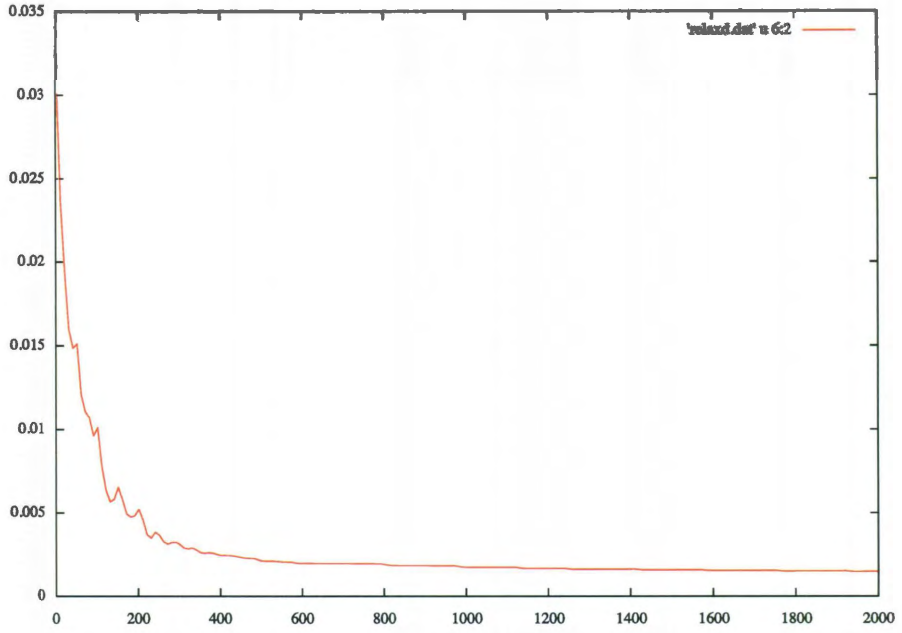

Figure 2.14 : Force imbalance curve of a typical friction code run. Horizontal axis shows iteration steps. Vertical axis shows the acceleration parameter.

code, the value of α is adjusted dynamically according to the following criteria. For the $(n+1)$ time step

$$\alpha^{(n+1)} = 2\alpha^{(n)} \tag{2.14}$$

if $N^{(n+1)} \geq N^{(n)}$, and

$$\alpha^{(n+1)} = \frac{1}{2}\alpha^{(n)} \tag{2.15}$$

if $N^{(n+1)} < N^{(n)}$. The α values corresponding to the result depicted above is shown in Figure 2.15.

To further increase the relaxation efficiency, a "ballistic method" is used. Analogous to a moving bead in a trough, when the system reaches a local potential minimum on its path, kinetic energy will drive the system farther apart from the minimal po-

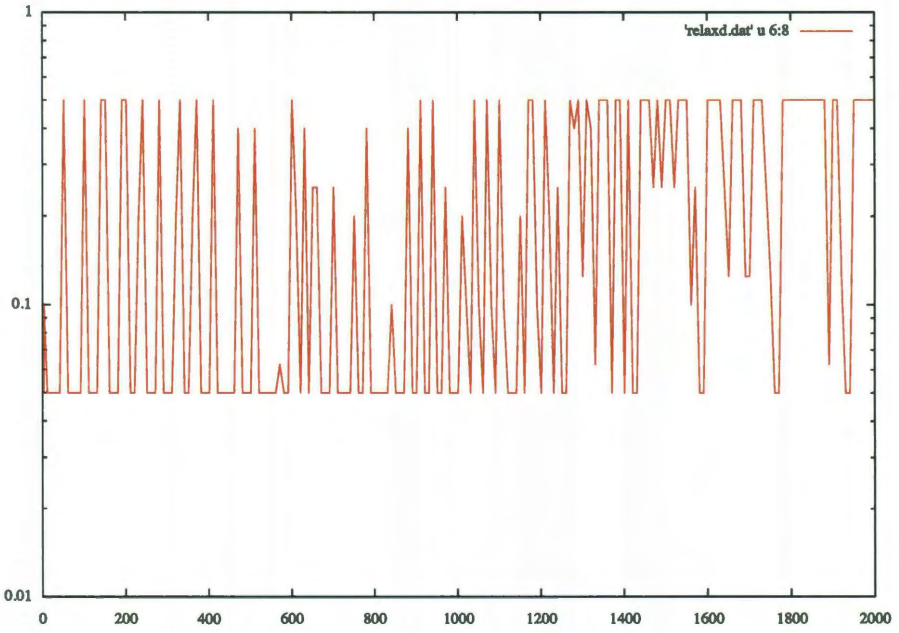

Figure 2.15 : Friction coefficient α curve corresponding to the result shown in Figure 2.14.

tential point and cause the computation to be wasted on the oscillations around the equilibrium point. To avoid this inefficiency, the friction code halts the system at exactly the point of kinetic energy maximum by setting the velocity to zero throughout the computational domain. Consequently, the system kinetic energy varies like the curve shown in Figure 2.16. The repeated sharp drops of kinetic energy are reflections of the ballistic method. Note as in Figure 2.14, the peaks of kinetic energy also dampen quickly within the first few hundreds steps.

Potential energy of the system continuously transforms into kinetic energy, and the latter is dissipated by the friction and the ballistic method. Ultimately, potential energy should decrease monotonically as the relaxation progresses. Figure 2.17 draws

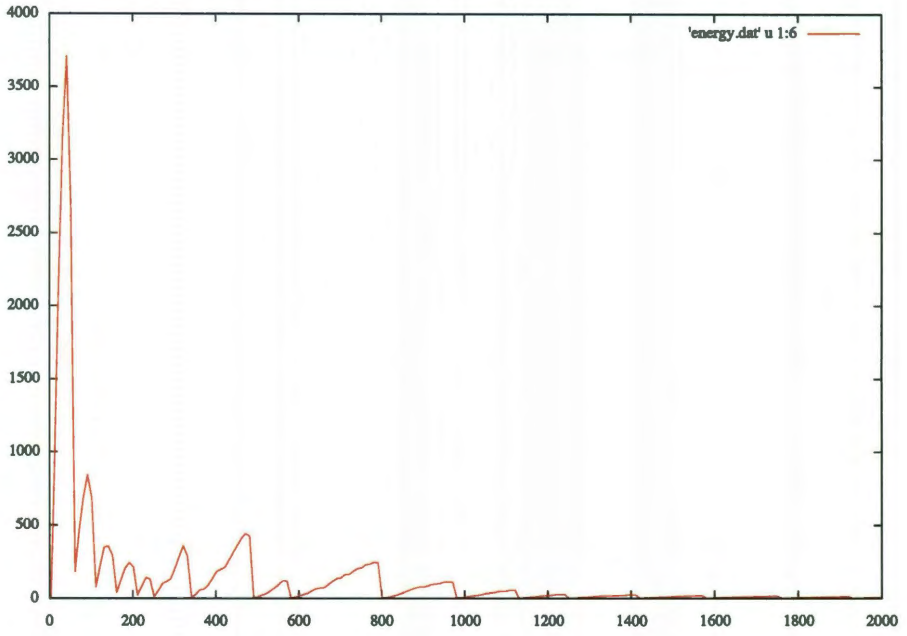

Figure 2.16 : Kinetic energy curve corresponding to the result shown in Figure 2.14.

the potential energy curve corresponding to the above result. The initial dramatic increase and the subsequent oscillations of potential energy are believed due to small numerical errors in the calculation of the magnetic field, which are emphasized in the energy calculation due to the squaring of the magnetic term [*Lemon et al.*, 2003 [22]]. Dipole magnetic field energy dominates the total potential energy, and is several orders of magnitude greater than the potential energy decrease during the relaxation. Therefore, numerical errors in the calculation can easily overwhelm the physical energy changes. After the most dynamic changes of the system in the first few hundreds time steps, the monotonic decrease of potential energy is then apparent.

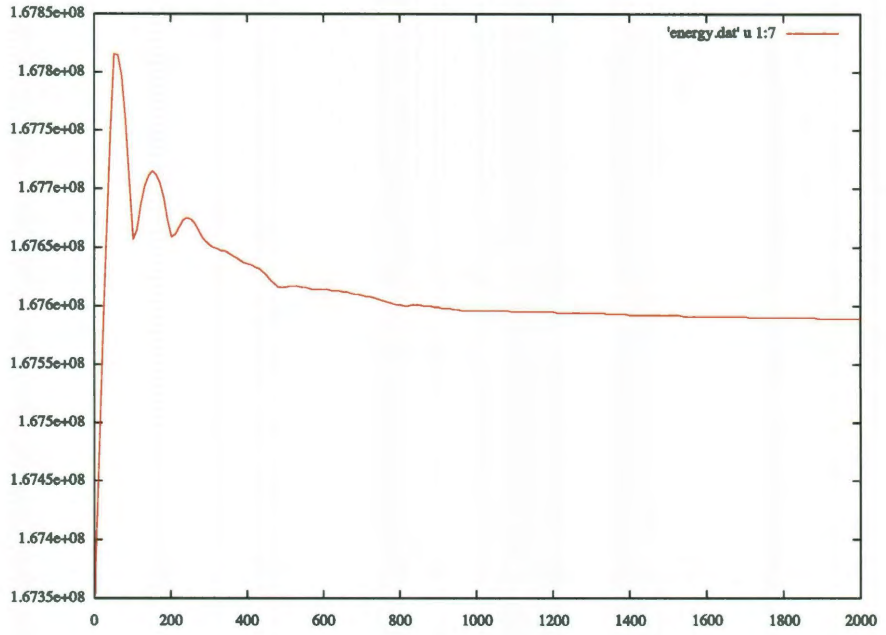

Figure 2.17 : Potential energy curve corresponding to the result shown in Figure 2.14.

2.5 The PV^{γ} correction

Many numerical algorithms for solving advection equations have been known to introduce numerical diffusion to the system. AB3 is amongst them. Numerical diffusion in MHD simulation causes magnetic field lines to slide through plasma, thereby violating the frozen-in flux condition (1.7). In the worst case, when the tail field lines are highly stretched and hence tearing-mode unstable, numerical diffusion could trigger the magnetic field reconnection, which subsequently changes the field line topology. Figure 2.18 exemplifies a plasmoid, which is a bulk of magnetized plasma with self-closed field lines, being generated in a friction code calculation. The optional PV^{γ} correction algorithm was designed intentionally to prevent this from happening, but its performance is unsatisfactory.

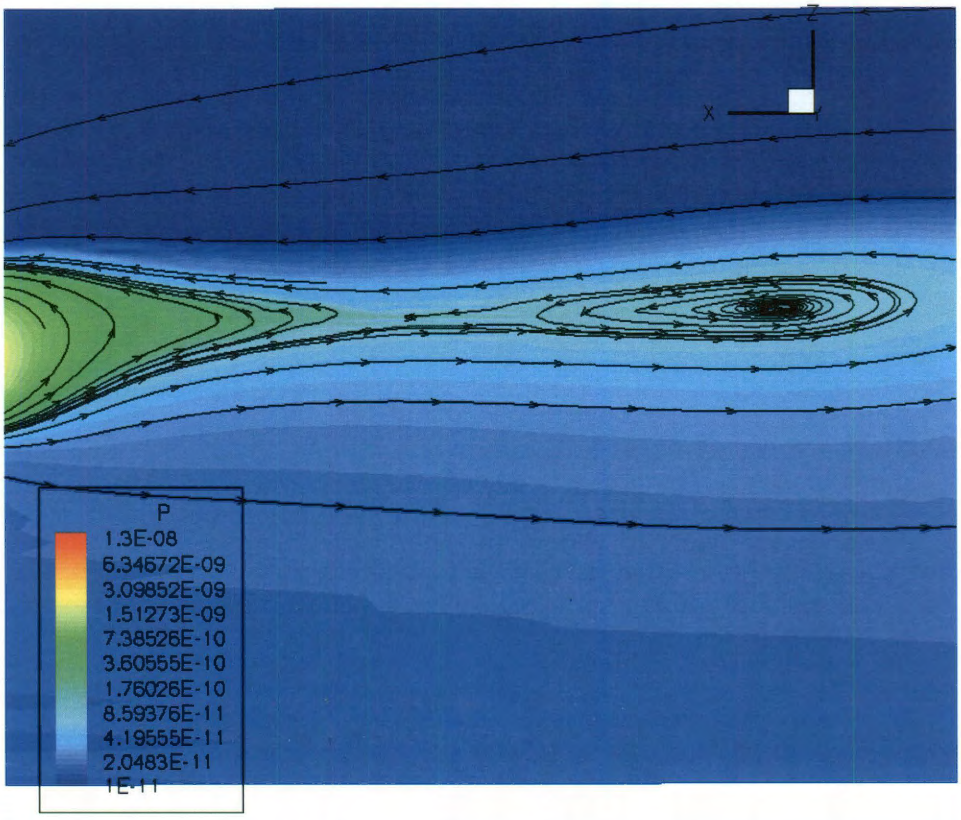

Figure 2.18 : A plasmoid was developed during the relaxation procedure due to numerical diffusion in a friction code run. Magnetic field model is T96 with 30° tilt angle, 1.5 nPa solar wind dynamic pressure and 5.0 Dst. Color code is pressure.

The frozen-in flux condition is derived from ideal MHD equations. Under the assumption of lossless convection, it is equivalent to the equation (1.21), that the quantity PV^{γ} is conserved for a flux tube. Because of this, one way to attenuate numerical diffusion is by explicitly enforcing the conservation of PV^{γ} during the computation. This is the idea behind the PV^{γ} correction. Near to the Earth, magnetic field is dominated by the Earth's dipole field, therefore, we believe the ionospheric footprints of field lines should not move during relaxation. Consequently, if we map all closed field lines' PV^{γ} values onto the ionosphere, this ionospheric PV^{γ} distribution should not change due to the conservation of PV^{γ} .

In numerical implementation, after the initial setup but before the relaxation procedure starts, we build a dense mesh on the northern ionosphere, and perform field line tracing for every mesh node to record the initial ionospheric PV^{γ} distribution. An example of such distribution is shown in Figure 2.19. In practice, this ionospheric mesh is not built just above the surface of the Earth, but on a sphere with radius 3 R_E. This is because, in the computational domain, grid space around the Earth (about 1/10 R_E) is not small enough compared to the size of the Earth, if we trace two different field lines from the tail all way down to the surface of the Earth, numerical error caused by the linear interpolation (Ref. subsection 2.1.1) will overwhelm the small distance between their footprints. Then after the relaxation begins, we routinely trace field lines for the closed magnetic field region grid nodes, calculate their PV^{γ} values, and compare with the initial PV^{γ} values obtained by referencing

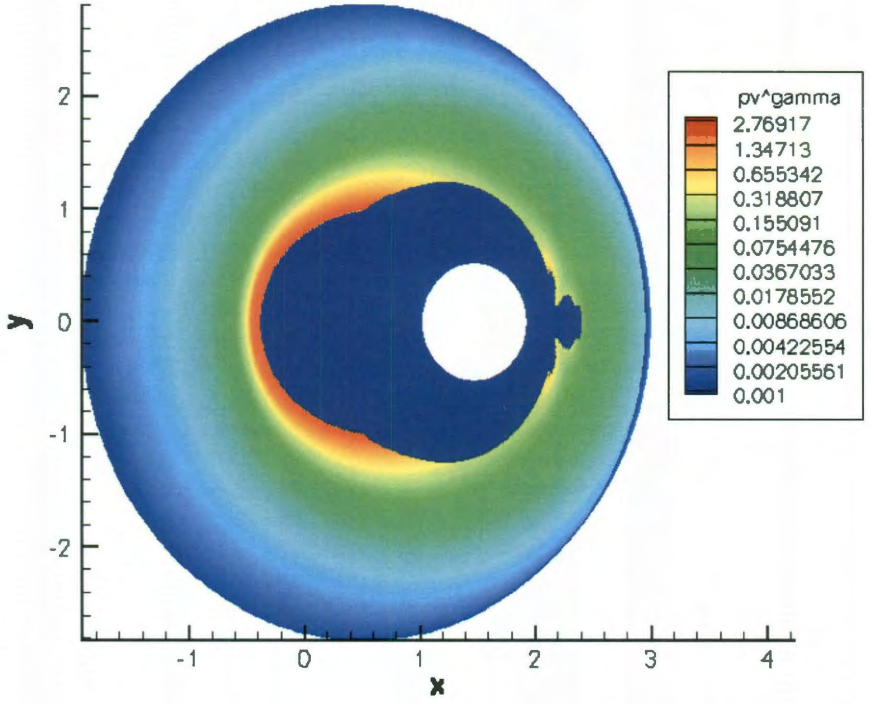

Figure 2.19 : PV^{γ} (in unit of $\mathrm{nPa}(\mathrm{R_E}/\mathrm{nT})^{5/3}$) distribution on the ionosphere domain. The domain covers an annular region of the reference sphere with radius 3 $\mathrm{R_E}$, from magnetic colatitude 10° to 70°. North magnetic pole lies at the center of the inner blank hole shown in this figure. The dark blue region between the blank hole and the outer colored region is the region contains open and tail lobe field line footprints, hence PV^{γ} is not defined there. The color map is shown in log scale, thus the gradient of PV^{γ} at high latitude is very steep. The domain looks oval rather than circular because the dipole is tilted toward GSM $+x$ direction and we are looking down along the z axis.

their ionospheric footprints in the ionospheric mesh. The pressure at a grid node is then corrected by

$$P_{new} = P_{old}\frac{(PV^{\gamma})_i}{(PV^{\gamma})_{old}} \tag{2.16}$$

where subscript *new* denotes for quantities after the PV^{γ} correction, *old* for quantities before the PV^{γ} correction, i for values referenced from the ionospheric mesh.

Despite the large computation amount brought by repeated field line tracings, test runs showed that the PV^{γ} correction could not effectively prevent magnetic reconnection from happening. The reason might be we did not perform correction frequently enough, and numerical diffusion between two corrections still triggered the reconnection. However, tracing tens of thousands field lines is highly time consuming. In addition, in some cases even though magnetic reconnection would not happen, the PV^{γ} correction can still cause problems. For example the relaxation procedure illustrated in Figure 2.20 features a "shock" generated by the PV^{γ} correction. At the 200 time steps, a region around -30 R_E was assigned higher pressure than its surroundings by the PV^{γ} correction. This is the region with minimal B_z in T96 model. Hence when we calculated the ionospheric distribution of PV^{γ} , overshooting of the field line tracer in this region caused a higher flux tube volume integration and thereby a higher ionospheric PV^{γ} value. When doing the PV^{γ} correction, field line tracings were started from grid nodes within the plasma sheet rather than from the ionosphere, and the overshooting was smaller. Therefore, the PV^{γ} correction erroneously thought the PV^{γ} value in this region was lowered during relaxation and

thus assigned it a higher pressure. In the picture of bubble and blob [*Yang et al.*, 2010 [37]], a blob was generated and subsequently a bubble developed Earthward of it, as shown in Figure 2.21. In a comparison run with identical initial setups but with the PV^{γ} correction turned off, such structures did not show up, see Figure 2.22. To fix this problem, a better field line tracer or a higher grid resolution might be needed.

2.6 Summary and future work

In this chapter, we described the full suite of assembling parts of the new version of the friction code. Among these, the magnetic field line tracer is the most fundamental and most frequently used. The field line tracer is responsible in the new friction code for locating the curved neutral sheet, classifying different magnetic field regions, setting up initial pressure and integrating the flux tube volumes. Therefore, the quality of field line tracings affects the quality of the friction code directly.

In section 2.2, we discussed the generation of stretched Cartesian grid, and the classification of computational domain according to field line topologies, which is a new feature of the friction code. The magnetic field regions could on one hand provide accurate positioning of the magnetopause, hence solving the magnetopause-crossing equilibrium problem that existed in the old friction code, and on the other hand greatly improved the efficiency of the PV^{γ} correction by eliminating redundant calculations.

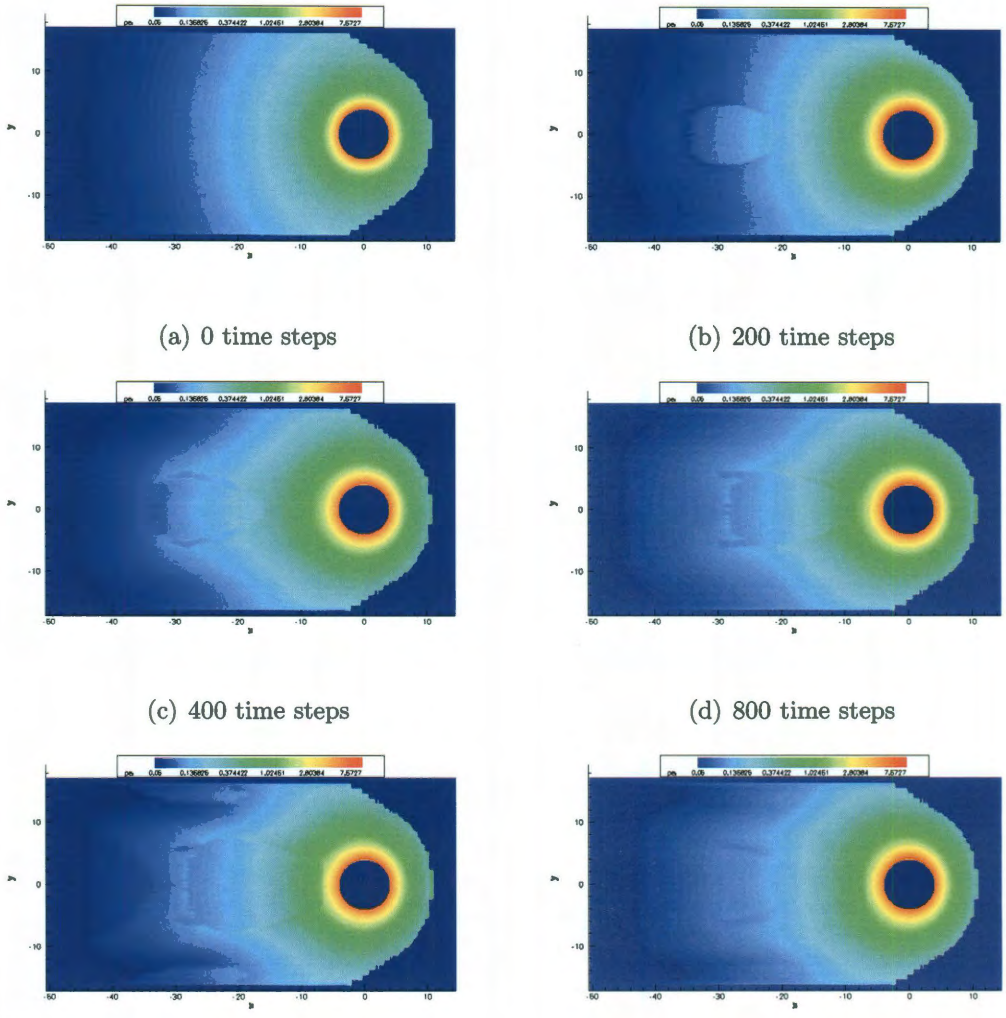

(a) 0 time steps

(b) 200 time steps

(c) 400 time steps

(d) 800 time steps

(e) 1500 time steps

(f) 2000 time steps

Figure 2.20 : A "shock wave" was generated by the PV^{γ} correction during relaxation. Color map shows the pressure distribution in the neutral sheet projected onto the xy plane.

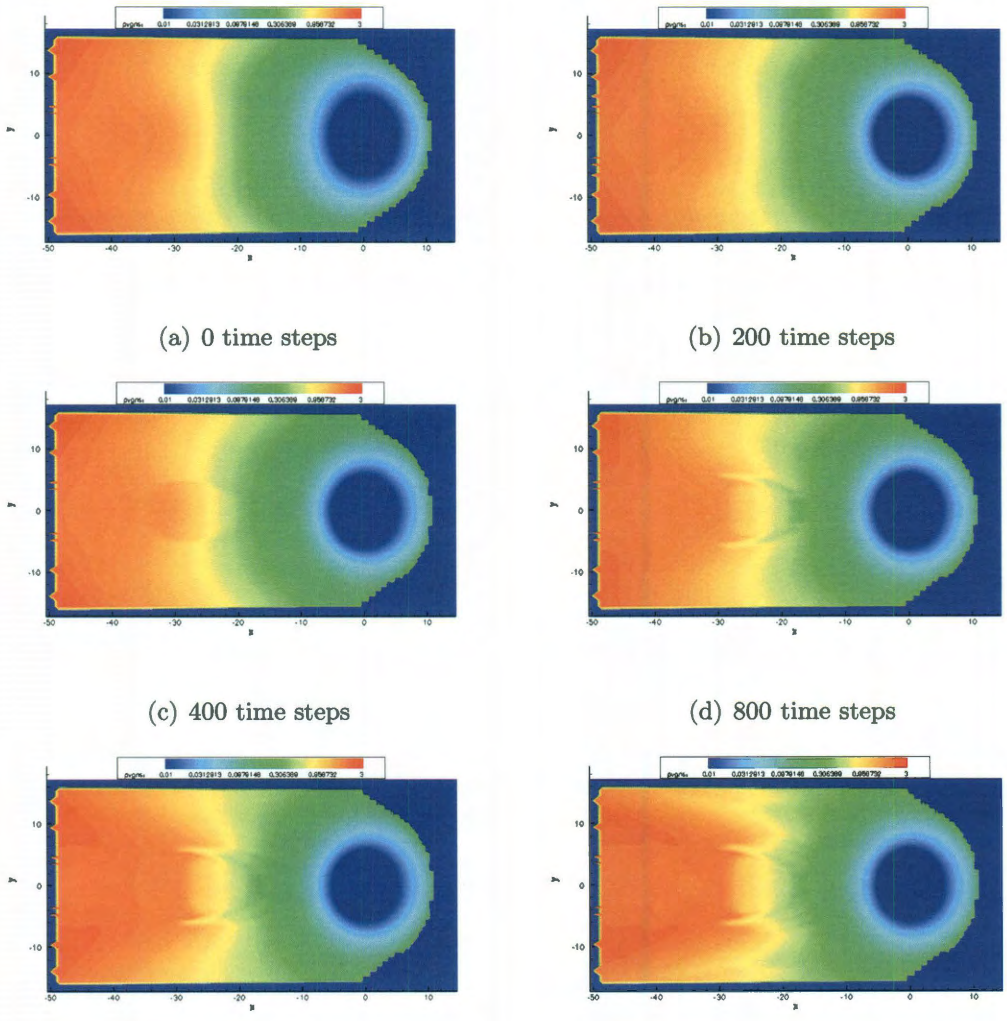

(a) 0 time steps

(b) 200 time steps

(c) 400 time steps

(d) 800 time steps

(e) 1500 time steps

(f) 2000 time steps

Figure 2.21 : The PV^{γ} values in the neutral sheet corresponding to Figure 2.20

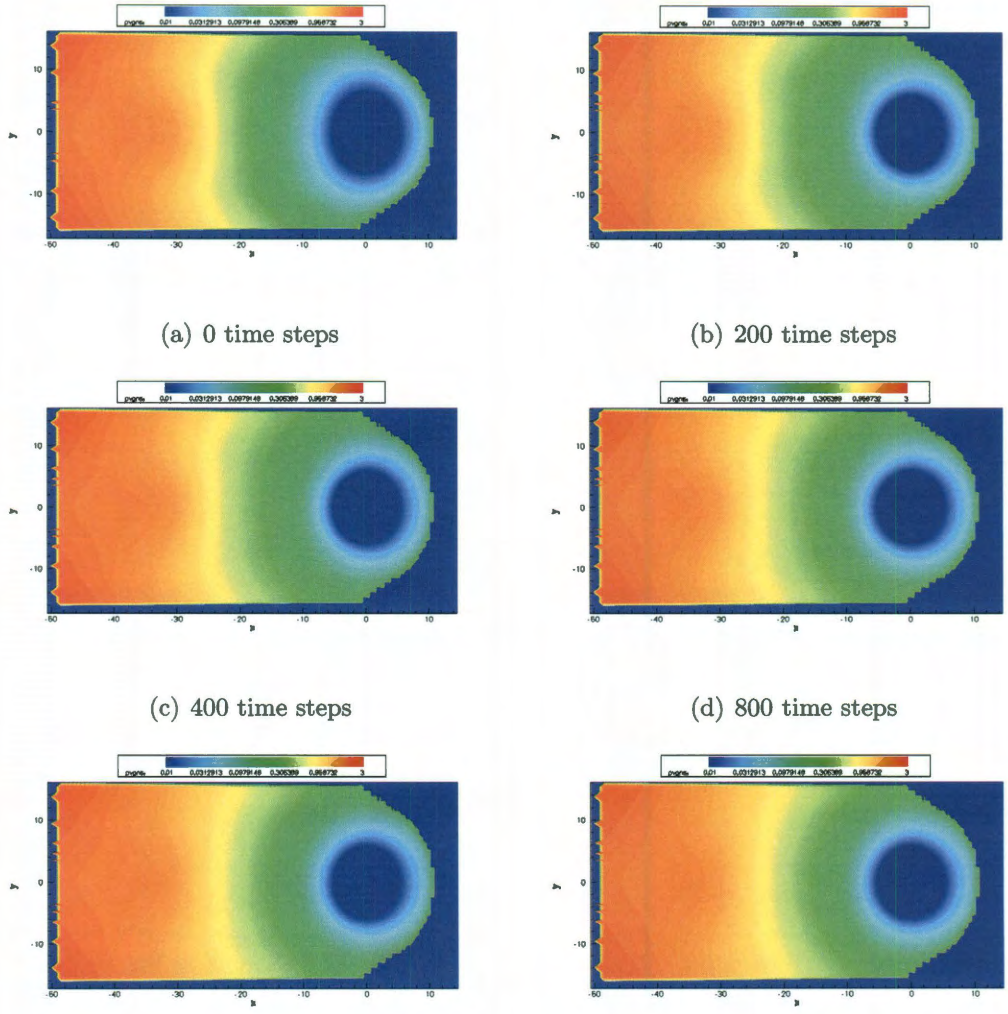

(a) 0 time steps

(b) 200 time steps

(c) 400 time steps

(d) 800 time steps

(e) 1500 time steps

(f) 2000 time steps

Figure 2.22 : The PV^{γ} values in the neutral sheet for the comparison run with identical initial conditions as the one shown in Figure 2.21, except this one turned the PV^{γ} correction off. The bubble and blob structure manifested in Figure 2.21 does not show up here.

Subsequently, the boundary conditions used in the friction code and numerical algorithms solving the MHD equations were described. Assessment of the relaxation procedure revealed that, by the introduction of artificial friction and the use of the "ballistic method", potential energy is indeed systematically dissipated, and the friction code is capable of reducing the force imbalance to less than 1/10 of the initial value, with arbitrary choices of dipole tilt angle and IMF conditions. This is a significant improvement to the previous version of the friction code.

Lastly in this chapter, we discussed numerical diffusion in the friction code algorithm, and one possible way to mitigate it the PV^{γ} correction. Though simple in idea, practical implementation demonstrated that the successful operation of the PV^{γ} correction depends critically on the precision of our field line tracer. Therefore, improving the current field line tracing algorithm represents one of the future development of the friction code.

Chapter 3

Flux Tube Volume Estimation

3.1 Background

The theory of plasma transport in Earth's plasma sheet critically depends on the entropy parameter PV^{γ} . *Bernstein et al.* [1958] [1] gives the criterion for plasma sheet interchange instability as

$$(PV^{\gamma})' \left(V' - P'\mu_0 \int \frac{ds}{B^3} \right) < 0 \tag{3.1}$$

where primes indicate spatial derivatives. Moving tailward in plasma sheet, flux tube volume V increases while pressure P decreases, thus terms in the second parenthesis add. Then (3.1) indicates that the plasma sheet is unstable if PV^{γ} decreases tailward. If one measures V and P from statistical models, PV^{γ} normally increases tailward, as illustrated in Figure 3.1, so the statistically averaged plasma sheet is generally interchange stable [*Xing and Wolf*, 2007 [36]]. On the other hand, Figure 3.1 shows that the value of PV^{γ} increases by at least one order of magnitude from the near Earth plasma sheet to the far tail; however, according to the adiabatic convection theory and the conservation of PV^{γ}, the distribution of PV^{γ} should be roughly uniform in the tail. The inconsistency between statistical models and theory is called the "pressure balance inconsistency" [*Wolf et al.*, 2009 [34]]. Although force-balanced magnetosphere configurations with approximate uniform entropy in the tail have been

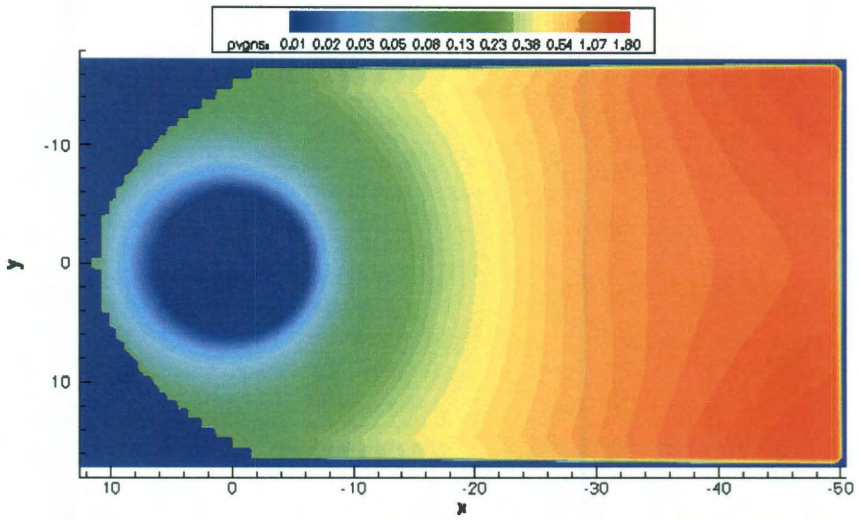

Figure 3.1 : Distribution of PV^{γ} in the neutral sheet under equilibrium, based on T96 magnetic field model and TM03 pressure model, for solar wind dynamic pressure 1.5 nPa, IMF $B_y = 0$ nT and $B_z = 2$ nT, Earth dipole tilt angle 0°. PV^{γ} is shown in unit of $\mathrm{nPa}(\mathrm{R_E}/\mathrm{nT})^{5/3}$.

obtained, for example the 2D magnetotail calculation by *Hau* [1991] [16], these equilibrium configurations exhibit highly stretched tail magnetic field lines featured with a deep B_z minimum in the near Earth tail, which is absent in statistical models. This fact suggests that in reality these highly stretched configurations are either rare or of short duration. One possible explanation of this inconsistency might be the transport of bubbles and blobs [*Chen and Wolf*, 1993 [11] and *Wolf et al.*, 2009 [34]], whereby a bubble, a bundle of flux tubes with lower PV^{γ} than their surroundings, convects Earthward and a blob with higher PV^{γ} moves tailward. A statistical model cannot describe this kind of dynamic changes in flux tube volume; neither can spacecraft measure it directly, therefore, the ability to estimate PV^{γ} is desirable to better

understand plasma sheet dynamics.

Wolf et al. [2006] [33] proposed a simple but elegant empirical formula (Wolf formula) to estimate the flux tube volume, and hence PV^{γ}, from single-spacecraft measurements in the magnetotail. Their formula is based on the solution of the 2D linear Grad-Shafranov equation (1.34). Away from the Earth, the Dirac-δ function source term in equation (1.40) vanishes, namely,

$$\nabla^2 A(x,z) + k^2 A(x,z) = 0 \tag{3.2}$$

Its solution can be written as

$$A(x,z) = -A_0 \cos(\frac{\pi z}{2z_0}) \exp(-\lambda x) \tag{3.3}$$

and from (1.38)

$$B_z = \frac{\partial A}{\partial x} = -\lambda A \tag{3.4}$$

By the definition of flux tube volume (1.17), V is integrated by

$$V(A) = \int \frac{ds}{B(s)} = \int_{-z_0}^{z_0} \frac{dz}{B_z(A)} = \frac{\pi/\lambda}{\sqrt{B_z(A)^2 + 2\mu_0 P(A)}} \tag{3.5}$$

which states that the flux tube volume is proportional to a characteristic length in the x dimension π/λ, and the $-1/2$ power of the total pressure in the equatorial plane. The real magnetosphere is not 2D, and in the inner and middle plasma sheet B_z does not actually decline exponentially down the tail. *Wolf et al.* accommodated these facts by assuming that the characteristic length has a power law dependence on measurable parameters and thereby wrote their empirical formula

$$V_E(x,y) = \frac{10^C (\sqrt{x^2+y^2})^D (B_{zE}(x,y))^F}{\sqrt{B_{zE}(x,y)^2 + 2\mu_0 P_E(x,y)}} \tag{3.6}$$

where subscript E denotes for quantities measured in the equatorial plane (or neutral sheet in the general case), (x, y) are the GSM coordinates of the measurement, and C, D and F are parameters determined by calibration against a series of equilibrated statistical magnetospheres.

In practice, spacecraft usually do not stay in the equatorial plane, but those equatorial quantities in (3.6) still need to be estimated from local measurements. Let z now denote the distance in z direction of the observing spacecraft from the neutral sheet, $V_E(x, y; z)$ the estimate of $V_E(x, y, 0)$, and $P_E(x, y; z)$ and $B_{zE}(x, y; z)$ the estimates of $P(x, y, 0)$ and $B_z(x, y, 0)$, from measurements made at (x, y, z). *Wolf et al.* estimated the equatorial B_{zE} by application of (3.4) and derived

$$B_{zE}(x, y; z) = B_z(x, y, z)\sqrt{1 + \frac{B_r(x, y, z)^2}{B_z(x, y, z)^2 + 2\mu_0 P(x, y, z)}} \tag{3.7}$$

where $B_r = \sqrt{B_x^2 + B_y^2}$. And the equatorial P_E is estimated using the 1D force balance modified by a "distance" from the equatorial plane

$$P_E(x, y; z) = \left(P(x, y, z) + \frac{B_r(x, y, z)^2}{2\mu_0}\right) 10^{-G\frac{B_r(x,y,z)}{B_z(x,y,z)}} \tag{3.8}$$

in which G is a calibration parameter.

The Wolf formula provides the first practical means of estimating the local PV^γ value from *in situ* measurements, thus is heavily used in the space physics community [*e.g. Yang et al.*, 2010 [37] and *Birn et al.*, 2009 [6]]. Despite its simpleness and successfulness, it has a few limitations. First, the accuracy of Wolf formula becomes worse closer to the Earth, because the formula was derived from an infinitely long

magnetotail model. Second, in the inner magnetosphere, the effect of Earth dipole tilt is no longer negligible, and Wolf formula does not take into account of this effect. Tests of Wolf formula against dipole-tilted magnetosphere equilibriums generated by the new version of the friction code are summarized in Table 3.1 and Table 3.2. In these tables, the ratio B_r/B_z characterizes the distance of measurement from the neutral sheet; the symbol $\Delta \log Q$ is the abbreviation of the log-scale root-mean-square (RMS) error defined by

$$\Delta \log Q = \sqrt{\left\langle \left(\log_{10} \frac{Q_E(x,y;z)}{Q_{N.I.}(x,y,0)} \right)^2 \right\rangle} \tag{3.9}$$

where "$N.I.$" stands for "numerical integration". The average is taken over the measurements within a 45° wedge centered on midnight and between 6 and 20 R_E from the Earth, with their B_r/B_z lying in a certain bin. Generally, the RMS error of Wolf formula increases with both B_r/B_z and the Earth dipole tilt.

3.2 Theoretical generalization of the tail flux tube volume calculation

A rich series of flux tube volume integrations can be obtained from generalizations of the 2D linear Grad-Shafranov equation. The actual magnetotail is finite in length rather than being infinitely extended in the calculation of equation (3.5). If we were to terminate the integration at some finite $x = x_0$ instead of extending to infinity, the

Table 3.1 : Values of $\Delta \log V_E$ for different tilt angles and B_r/B_z bins

Bin\Tilt	0°	10°	20°	30°	Average
0.0-0.5	0.0684	0.0675	0.0616	0.0597	0.0643
0.5-1.0	0.0572	0.0588	0.0718	0.1058	0.0732
1.0-1.5	0.0498	0.0664	0.1072	0.1602	0.0959
1.5-2.0	0.0489	0.0710	0.1246	0.1935	0.1095
2.0-2.5	0.0456	0.0805	0.1360	0.1976	0.1149
2.5-3.0	0.0451	0.0781	0.1397	0.2053	0.1170
3.0-3.5	0.0466	0.0804	0.1369	0.1949	0.1147
3.5-4.0	0.0457	0.0785	0.1298	0.1919	0.1115
Average	0.0509	0.0727	0.1134	0.1636	0.1002

Table 3.2 : Values of $\Delta \log PV^{\gamma}$ for different tilt angles and B_r/B_z bins

Bin\Tilt	0°	10°	20°	30°	Average
0.0-0.5	0.0637	0.0596	0.0575	0.0692	0.0625
0.5-1.0	0.0780	0.0759	0.0793	0.1034	0.0842
1.0-1.5	0.0913	0.0905	0.1018	0.1363	0.1050
1.5-2.0	0.1017	0.1027	0.1183	0.1660	0.1222
2.0-2.5	0.1016	0.1084	0.1357	0.1768	0.1306
2.5-3.0	0.1038	0.1103	0.1396	0.1932	0.1367
3.0-3.5	0.1065	0.1145	0.1484	0.1900	0.1398
3.5-4.0	0.1021	0.1119	0.1480	0.1914	0.1384
Average	0.0936	0.0967	0.1161	0.1533	0.1149

flux tube volume would then be

$$V(A) = \frac{2\arccos\left(\sqrt{\frac{P(A)}{P_0(x_0)}}\right)}{\lambda\sqrt{B_z(A)^2 + 2\mu_0 P(A)}} \tag{3.10}$$

where $P_0(x_0)$ is the thermal pressure in the neutral sheet at x_0. Compared with π/λ in (3.5), the arccos factor in (3.10) gives a rescaled characteristic distance in the x direction.

A second modification is, instead of assuming a quadratic dependence of P on A, we assume a more general functional form

$$P(A) = \frac{k^2}{2\mu_0}A^2 + \frac{a}{\mu_0}A + \frac{b}{\mu_0} \tag{3.11}$$

By completing the square, equation (3.11) can be reformed to

$$P(A') = \frac{k^2}{2\mu_0}A'^2 - \frac{a^2}{2\mu_0 k^2} + \frac{b}{\mu_0} \tag{3.12}$$

with

$$A' = A + \frac{a}{k^2} \tag{3.13}$$

Define

$$P'(A') = P(A') + \frac{a^2}{2\mu_0 k^2} - \frac{b}{\mu_0} \tag{3.14}$$

and replace (3.11) into Grad-Shafranov equation (1.34), we find that the linear equation of A' has exactly the same form as equation (3.2). Hence, the modified flux tube volume reads

$$V = \frac{\pi/\lambda}{\sqrt{B_z^2 + 2\mu_0 P'}} = \frac{\pi/\lambda}{\sqrt{B_z^2 + 2\mu_0(P + \Delta P)}} \tag{3.15}$$

in which

$$\Delta P = \frac{a^2}{2\mu_0 k^2} - \frac{b}{\mu_0} \tag{3.16}$$

The physical meaning of this modification is, when b is less than zero, plasma sheet thermal pressure reaches zero at some finite A, thereby truncating the plasma sheet at some finite distance in the tail.

Another modification comes from the work by *Voigt* [1986] [32] and *Hilmer and Voigt* [1987] [18], who added an IMF B_y into the 2D Grad-Shafranov equation. According to the divergence-free condition and Coulomb gauge of magnetic field, it is shown [*Hilmer and Voigt*, 1987 [18]] that B_y has to be a function of A only. For the linearization of the equation, we may choose the form

$$B_y(A) = hA + B_{yc} \tag{3.17}$$

where B_{yc} is a background B_y, the B_y value in the tail lobes. With the presence of B_y, the Grad-Shafranov equation (1.34) becomes

$$\nabla^2 A + \frac{d}{dA}\left(\mu_0 P(A) + \frac{1}{2} B_y(A)^2\right) = 0 \tag{3.18}$$

Inserting into (3.18) the quadratic form of $P(A)$ (1.41) and (3.17), (3.18) transforms to an inhomogeneous Helmholtz equation. By the solution of this equation, the flux tube volume can be calculated by

$$V = \frac{\pi/\lambda}{\sqrt{B_z^2 + B_y^2 + 2\mu_0 P - \dfrac{k^2}{k^2 + h^2} B_{yc}^2}} \tag{3.19}$$

In (3.19), B_y appears of equal rights with B_z, which is not surprise. The term with B_{yc} acts like the ΔP in (3.15) and (3.16), except that here it is negative semi-definite.

The asymptotic magnetotail equilibrium theory (Ref. Subsection 1.2.2) also provides an analytical calculation of flux tube volume under simplified situations. Assume that the total pressure P_{tot} is only a function of the distance $r = \sqrt{(x-x_0)^2 + (y-y_0)^2}$ to a remote reference pole (x_0, y_0) Sunward of the Earth, with x_0 the order of 100 R_E and $y_0 \ll x_0$ [*Birn*, 1979 [2]]. Also assume that the Euler potential $\beta = \phi$ [*Birn*, 1987 [3]], where ϕ and r constitute a polar coordinate system originated at (x_0, y_0), which means every field line lies in a vertical plane specified by $\phi = const.$ An implication of this assumption is that field aligned current is a higher order quantity under the tail approximation, proved by *Birn et al.* [1977] [8]. Furthermore, assume the functional form of $P(\alpha, \beta)$ in equation (1.57) as

$$P(\alpha, \beta) = P_N \exp(-2\lambda(\beta)\alpha) \tag{3.20}$$

where $\lambda(\beta)$ is a free function that characterizes the thickness of the plasma sheet (see below), and P_N is a constant. Under these assumptions, the integration in (1.57) can be evaluated analytically and yields [*Birn*, 1987 [3]]

$$z(r, \phi) = z_0(r, \phi) \pm L(r, \phi) \cosh^{-1}\left(\sqrt{\frac{P_{tot}(r)}{P}}\right) \tag{3.21}$$

where

$$L(r, \phi) = \frac{1}{\lambda(\phi) r \sqrt{2\mu_0 P_{tot}(r)}} \tag{3.22}$$

represents the characteristic half width of the plasma sheet at position (r, ϕ).

To calculate the flux tube volume of the magnetic field line specified by (3.21), we

notice the equivalence of operators

$$\vec{B}\cdot\nabla = B\left(\frac{\partial}{\partial s}\right)_{(\alpha,\beta)} = \left(\frac{\partial}{\partial \tau}\right)_{(\alpha,\beta)} \tag{3.23}$$

in which s is the arc length along a field line and $d\tau$ the differential flux tube volume. With this operator, the general equilibrium problem equation (1.11) through (1.13) transform to a series of first order ODE's

$$\left(\frac{\partial x}{\partial \tau}\right)_{(\alpha,\beta)} = B_x \tag{3.24}$$

$$\left(\frac{\partial y}{\partial \tau}\right)_{(\alpha,\beta)} = B_y \tag{3.25}$$

$$\left(\frac{\partial z}{\partial \tau}\right)_{(\alpha,\beta)} = B_z \tag{3.26}$$

$$\left(\frac{\partial B_x}{\partial \tau}\right)_{(\alpha,\beta)} = \mu_0 \frac{\partial P_{tot}}{\partial x} \tag{3.27}$$

$$\left(\frac{\partial B_y}{\partial \tau}\right)_{(\alpha,\beta)} = \mu_0 \frac{\partial P_{tot}}{\partial y} \tag{3.28}$$

$$\left(\frac{\partial B_z}{\partial \tau}\right)_{(\alpha,\beta)} = \mu_0 \frac{\partial P_{tot}}{\partial z} \tag{3.29}$$

The 3D asymptotic theory assumes 1D pressure balance along the z direction, therefore P_{tot} is not a function of z, and from (3.29), B_z is constant along a field line, then from (3.26), z coordinate increases monotonically along a field line. Note the same conclusion is made from the 2D linear Grad-Shafranov model too, which can be seen from equation (3.4). From (3.21) and the conclusion that B_z is constant along a field line, the flux tube volume is readily integrated

$$V = \int \frac{ds}{B(s)} = \int \frac{dz}{B_z} = \frac{2L(r_0,\phi_0)}{B_z}\cosh^{-1}\left(\sqrt{\frac{P_{tot}(r_0)}{P}}\right) \tag{3.30}$$

where the integration is performed along a field line from $(r_0, \phi_0, z_{south}(r_0, \phi_0))$ to $(r_0, \phi_0, z_{north}(r_0, \phi_0))$, in which r_0 is a distance as near to the Earth as the tail approximation applies. Inserting (3.22) into (3.30), we obtain

$$V = \frac{2}{\lambda(\phi_0) r_0 B_z \sqrt{2\mu_0 P_{tot}(r_0)}} \cosh^{-1}\left(\sqrt{\frac{P_{tot}(r_0)}{P}}\right) \tag{3.31}$$

$$= \frac{2}{\lambda(\phi_0) r_0 B_z \sqrt{2\mu_0 P}} \frac{1}{\chi} \cosh^{-1}(\chi) \tag{3.32}$$

with the dimensionless parameter defined as

$$\chi = \sqrt{\frac{P_{tot}(r_0)}{P}} \tag{3.33}$$

Two points are noticeable from the result (3.32). First, $z_0(r, \phi)$ does not appear, or in other words, in the tail approximation, flux tube volume does not explicitly depend on Earth dipole tilt angle. This is physically reasonable, because far from the Earth, the most significant effect of dipole tilt is to move the neutral sheet up or down, without altering the field line shape too much. Second, the $\sqrt{2\mu_0 P}$ term in (3.32) resembles (3.5), with B_z^2 ignored as it is a second order quantity in the tail approximation. The rest terms other than $\sqrt{2\mu_0 P}$ in (3.32) thus comprise a characteristic length in r direction.

3.3 Flux tube volume estimation from single spacecraft measurements at geosynchronous orbit

This section describes ongoing work of developing a flux tube volume estimation for geosynchronous orbit.

The gradient/curvature drift of plasma sheet particles becomes dominant from the Sunward $\vec{E} \times \vec{B}$ drift at about the distance of geosynchronous orbit (GEO) to the Earth on the nightside [*Korth et al.*, 1999 [20]]. Especially when geomagnetic activity is moderate or high, GEO can be partly or almost entirely out of the ion and electron Alfvén layer, as observed by the frequent detecting of plasma sheet ions and electrons by GEO satellites [*e.g. McComas et al.*, 1993 [23] and *Korth et al.*, 1999 [20]]. Particularly during storm times, magnetic field lines at GEO can be greatly stretched away from a dipolar shape and can extend well into the magnetotail. Therefore, the many GEO satellites routinely survey the inner edge of the plasma sheet and can provide continuous and valuable surveillance of the plasma sheet dynamics if flux tube volume and PV^{γ} should be estimated from their observations. This is the motivation of the flux tube volume estimation at GEO.

In contrast to the tail flux tube volume calculations described in the above sections, GEO is close to the Earth, and Earth's dipole field dominates the magnetic field configuration with a correction caused by the existence of plasma, or more specifically, by the moderate value ($\lesssim 1$) of plasma β parameter, which is defined as the ratio of thermal pressure to magnetic pressure:

$$\beta = \frac{2\mu_0 P}{B^2} \tag{3.34}$$

This is the difficulty of estimation the flux tube volume at GEO: the magnetic field is in the transitioning from one extreme, the dipole configuration, to another extreme, the magnetotail, and no analytical theory describes this transition region.

Chan et al. [1994] [10] solved the near Earth magnetosphere equilibrium problem by a local multi-scale perturbation method, and concluded that for a finite plasma pressure perturbation, to the first order of plasma β, the field line shape remains dipolar, but its local strength is modified by

$$\vec{B} = \vec{B}_d(1 - \frac{1}{2}\beta_d) \tag{3.35}$$

in which $\vec{B}_d$ is the zeroth order dipole field and β_d is given by

$$\beta_d = \frac{2\mu_0 P}{B_d^2} \tag{3.36}$$

Krasheninnikov et al. [1999] [21] derived an approximate analytic solution to the equilibrium problem that finite pressure plasma is confined by a point dipole field. In their solution, as plasma β approaches zero, to the first order of β, magnetic field reduces to

$$\vec{B} = \vec{B}_d(1 - \frac{512}{1001}\beta_E) \tag{3.37}$$

where β_E is the equatorial β value.

Intuitively, we may choose the flux tube volume of the unperturbed dipole field as a zeroth order approximation of that of GEO, that is

$$V_d = \frac{32}{35}\frac{L^4 R_E}{B_{EO}} \tag{3.38}$$

in which B_{EO} is the field strength in the magnetic equatorial plane on the surface of the Earth, and L is the distance of the field line's equatorial crossing point to the Earth, measured in unit of R_E. And by (3.35) and (3.37), since the field strength

is modified by β, so is the flux tube volume. Thus, we write the flux tube volume estimate as

$$V = V_d f(\beta_E) \tag{3.39}$$

with the functional form of f to be determined by comparisons with numerically calculated flux tube volume. To distinguish different field lines, we used the equatorial β value (or neutral sheet value in dipole-tilted case) β_E in (3.39). However, the Earth's dipole axis is inclined from the spin axis by 11° [*Kivelson and Russell*, 1995 [19]], so that GEO does not lie in the magnetic equatorial plane or the neutral sheet, GEO satellites cannot measure β_E directly. And β is not a constant along a field line. We need to estimate β_E from GEO spacecraft measurements first. Assuming that the spacecraft resides on a dipole field line, given the coordinates of a spacecraft, we are able to derive the L value of the assumed field line, and hence the value of derived β_E^*

$$\beta_E^* = \frac{2\mu_0 P}{B_E^{*2}} = \frac{2\mu_0 P}{(\frac{m}{L^3})^2} \tag{3.40}$$

where asterisk denotes that the quantity is derived. m is the Earth's dipole moment with the coefficient $\frac{\mu_0}{4\pi}$ absorbed in it, or equivalent to B_{EO} in (3.38). Inserting (3.40) and (3.38) into (3.39) then yields

$$V = \frac{32}{35}\frac{L^4 R_E}{m} f(\beta_E^*) \tag{3.41}$$

Note that, in (3.41) no measurement of magnetic field was used.

To test the validity of the proposition (3.41), we apply it to the equilibrated magnetosphere calculated by the friction code and scatter-plot f versus β_E^*, to see if

clear functional trend appears. We employed two methods of sampling data in the tests. Method one samples from an annular region between 4 and 9 R_E in the neutral sheet; and method two samples from a band on a sphere with radius 6.6 R_E that covers $\pm 11^\circ$ of elevation angle measured from the magnetic equator, as illustrated in Figure 3.2. When the dipole tilt angle is zero (as in Figure 3.2), the band covers exactly all the possible positions that a GEO spacecraft may take; when the dipole tilt is non-zero, the band covers more area than a GEO spacecraft may actually cover. For example in the extreme case when dipole tilt is $+34.5^\circ$, it is certain that the spin axis must be 23.5° inclined from the GSM z axis toward the Sun, and there is only one possible orbit in this case.

An example of test results of formula (3.41) using sampling method one is plotted in Figure 3.3. The equilibrium magnetosphere used in this and the following tests was computed from T96 magnetic field model and TM03 pressure model, with initial parameters: dipole tilt angle 30°, IMF B_y 0 nT, IMF B_z 2 nT, Dst -20 nT and solar wind dynamic pressure 1.5 nPa. In Figure 3.3, a clear trend of f approaching unity is seen, meaning that when β_E^* is small, the dipole field flux tube volume is a good approximation. As β_E^* gets larger, data points show significant magnetic local time dependence. Figure 3.4 illustrates the test result of (3.41) using sampling method two. In contrast to Figure 3.4, no clear and uniform trend is shown in this figure. Therefore, the simple dipole approximation is not quite a suitable method for the estimation of flux tube volume at GEO.

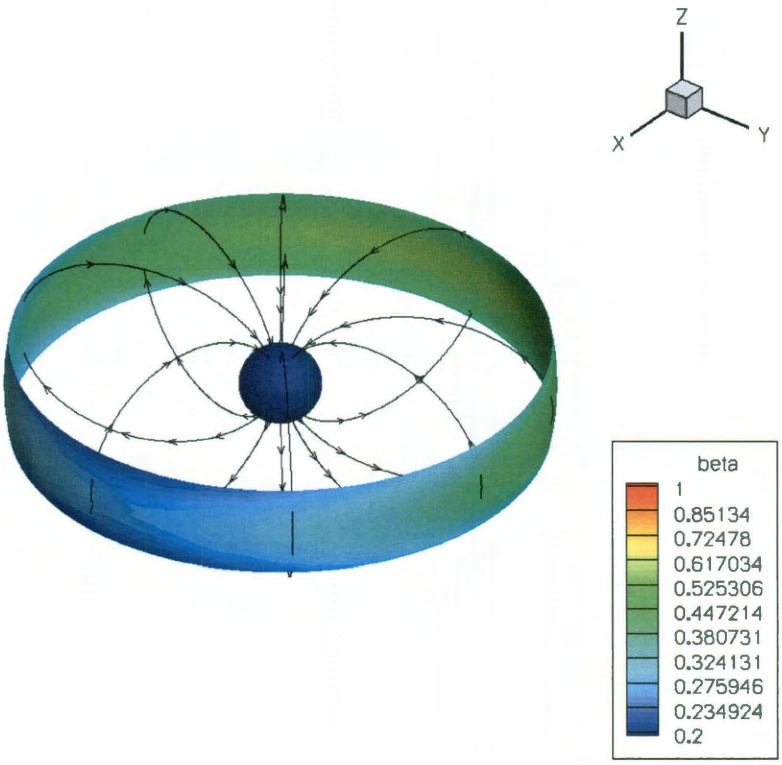

Figure 3.2 : Sampling area of the GEO. The area is a band on a sphere with radius 6.6 R_E that covers $\pm 11°$ of elevation angle measured from the magnetic equator. Color on the band shows the plasma β distribution in an example friction code result.

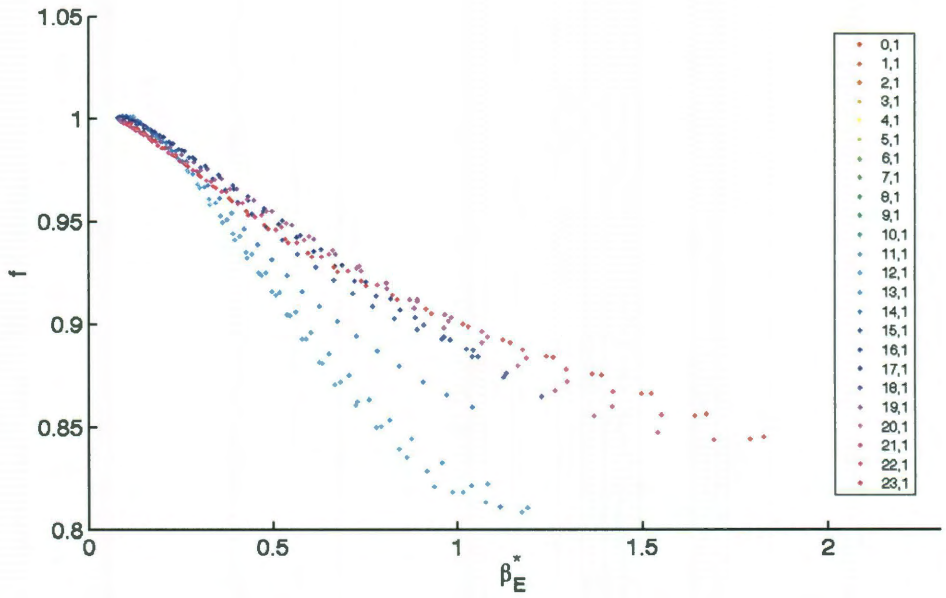

Figure 3.3 : Scatter plot of f versus β_E^* of formula (3.41) using sampling method 1. Each dot represents an evaluation of f from numerical flux tube volume integration. Color of the points shows different magnetic local times with 0 hour the mid-night. The number 1's in the legend after each local time are a byproduct of the plotting procedure, and is irrelevant in this and the following plots. As β_E^* approaches to 0, f values converge to 1, which means numerically calculated flux tube volume values approach to the estimations made by dipole field.

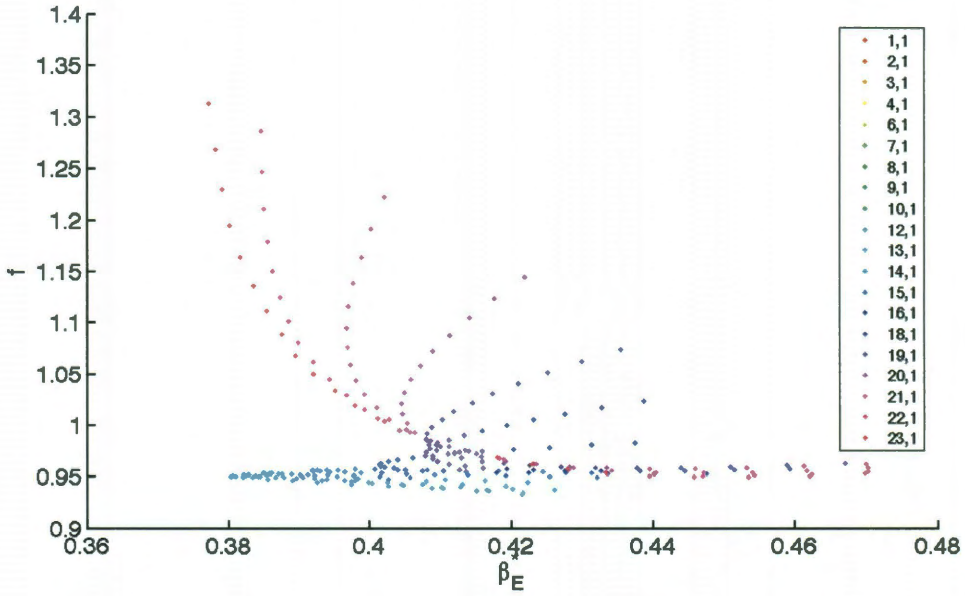

Figure 3.4 : Scatter plot of f versus β_E^* of formula (3.41) using sampling method 2. Each dot represents an evaluation of f from numerical flux tube volume integration. Color of the points shows different magnetic local times with 0 hour the mid-night. No clear and uniform trend of distribution is found in this test.

We notice that when plasma is present, a dipole flux tube is not only affected by the pressure along itself, but also by the diamagnetic effect of the plasma Earthward of it and the current systems outside. So, in light of (3.41), we introduce the concept of effective dipole moment m_{eff} for each sampling point, which is defined as

$$m_{eff} = \frac{Br^3}{\sqrt{3\cos^2(\theta)+1}} \tag{3.42}$$

where B is the field strength at the sampling point, r is the radial distance from the center of the dipole, and θ is its magnetic colatitude, or the polar angle in the geomagnetic dipole coordinate system (abbreviated MAG, a polar spherical system with its pole coincide with the dipole axis). Equation (3.42) says that the magnetic field strength at the sampling point is effectively caused by a dipole with moment m_{eff}. Replacing m by m_{eff} in (3.40) and (3.41), and repeating the test procedures aforementioned, the results are plotted in Figure 3.5 and Figure 3.6. Figure 3.6 clearly shows a better alignment of data points than that in Figure 3.4; but there seem to exist two trends, one is a steeper descent of the mid-night data, and the other a slower and seemingly linear variation for the rest of the data. Examination (not shown here) of the neutral sheet crossing points of the field lines sampled in Figure 3.6 revealed that those mid-night points with high f values are actually associated with the field lines extending farthest into the tail.

Yet one may still ask the question that why formula (3.41) gives good ordering of points when the data are sampled from the neutral sheet, but much worse when they are sampled in the GEO band. A possible answer might be that the neutral sheet is

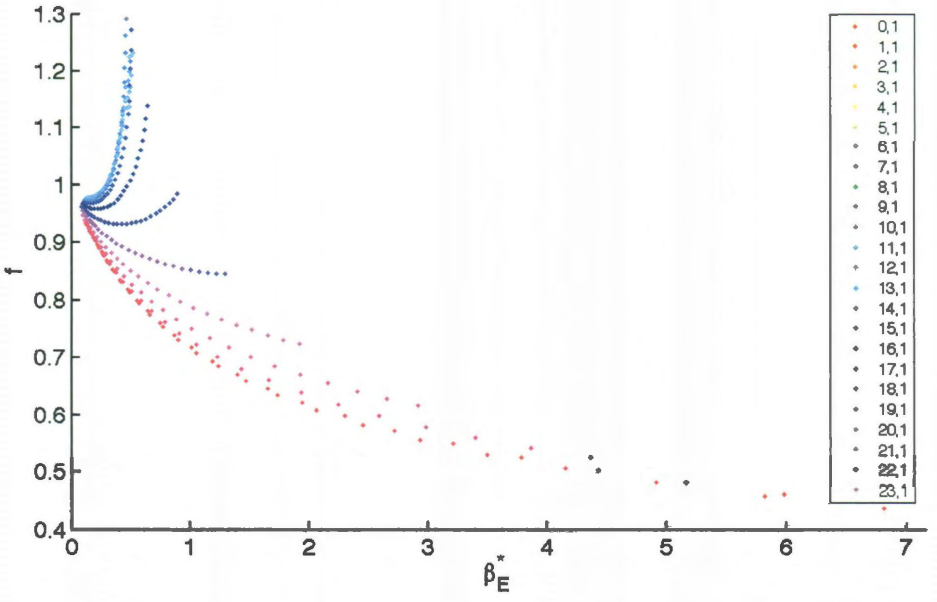

Figure 3.5 : Scatter plot of f versus β_E^* of formula (3.41) with effective dipole moment using sampling method 1. Color of the points shows different magnetic local times with 0 hour the mid-night. Similar to Figure 3.3, the convergence of f is also seen here.

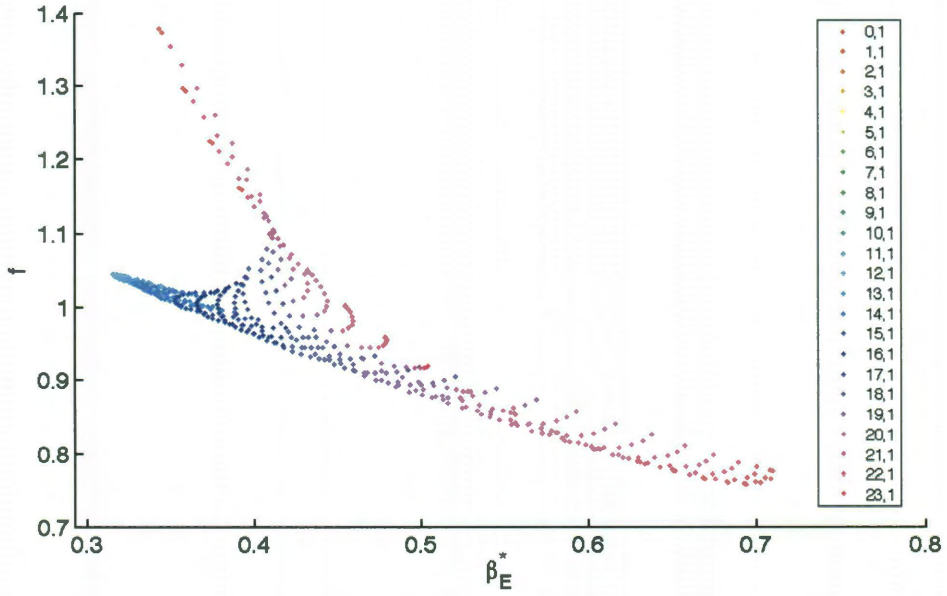

Figure 3.6 : Scatter plot of f versus β_E^* of formula (3.41) with effective dipole moment using sampling method 2. Color of the points shows different magnetic local times with 0 hour the mid-night. Unlike the plot in Figure 3.4, a better trend of data is shown in this figure.

unique from other places because magnetic field only has a z component there. This suggests that B_z may play a more important role than the other two components. Indeed, the z direction of GSM coordinate system is not only determined by the Earth's dipole, but also by the direction of the solar wind. And the importance of B_z is even more significant in the magnetotail where the effect of dipole is small, as can be seen from the flux tube volume calculations for the tail field lines (Ref. section 3.2). Following this, we further replaced the total B in (3.40), (3.41) and (3.42)by B_z, thereby the flux tube volume estimate finally becomes

$$V = \frac{32}{35}\frac{L^4\sqrt{3\cos^2(\theta)+1}R_E}{r^3 B_z} f\Big(\frac{L^6\big(3\cos^2(\theta)+1\big)}{r^6}\frac{2\mu_0 P}{B_z^2}\Big) \tag{3.43}$$

$$= \frac{32}{35}\frac{r\sin^{-2}(\theta)g(\theta)R_E}{B_z} f\big(g^2(\theta)\beta_z\big) \tag{3.44}$$

in which β_z is defined as

$$\beta_z = \frac{2\mu_0 P}{B_z^2} \tag{3.45}$$

and the function $g(\theta)$ writes

$$g(\theta) = \frac{\sqrt{3\cos^2(\theta)+1}}{\sin^6(\theta)}\ , \quad (0<\theta<\pi) \tag{3.46}$$

A graph of $g(\theta)$ is plotted in Figure 3.7. When the sampling is done in the magnetic equatorial plane, $\theta = \pi/2$, and $g(\theta) = 1$; as the sampling point moves away from the magnetic equatorial plane, $g(\theta)$ increases in both directions. Note, by doing this B_z replacement, we did not alter the concept of effective dipole moment, but only used the z component of the magnetic field caused by m_{eff}.

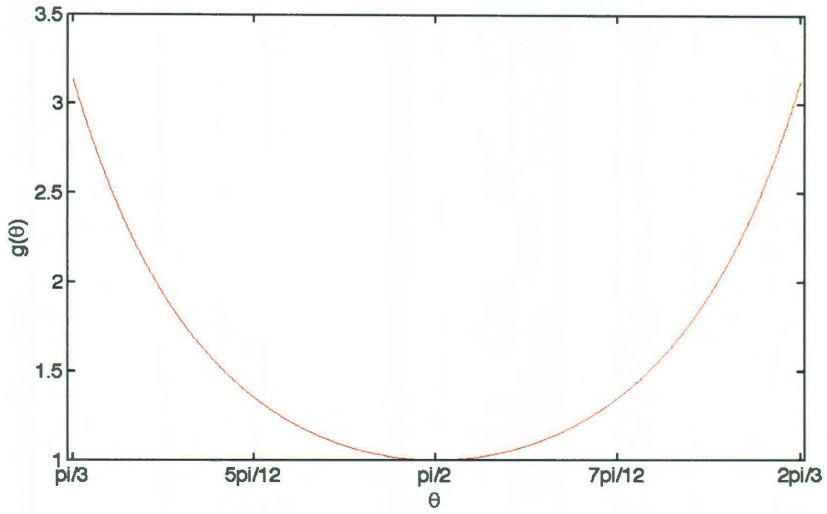

Figure 3.7 : Graph of $g(\theta)$.

Test results of formula (3.44) using the same equilibrated magnetosphere for samplings in the neutral sheet are shown in Figure 3.8 and Figure 3.9. β_E^* in these illustrations represents $g^2(\theta)\beta_z$, the argument of the function f. In Figure 3.8, the values of f do not converge to one number as did in Figure 3.3 and 3.5, when β_E^* approaches to zero. This reflects the fact that our replacement of B by B_z in formula (3.44) is not quite appropriate as the field line has a dipolar shape. The high β_E^* tail in this figure resembles the β_z dependence predicted by the 2D Grad-Shafranov model, which is $(1+\beta_z)^{-1/2}$ as can be seen from equation (3.5) by moving $B_z(A)$ out of the square root. A log-log scale plot of the data in Figure 3.8 is reproduced in Figure 3.9, which confirms the power law dependence of f on $(1+\beta_E^*)$, but the slope is slightly greater than $-1/2$.

Test results for formula 3.44 for samplings on the GEO band are shown in Figure

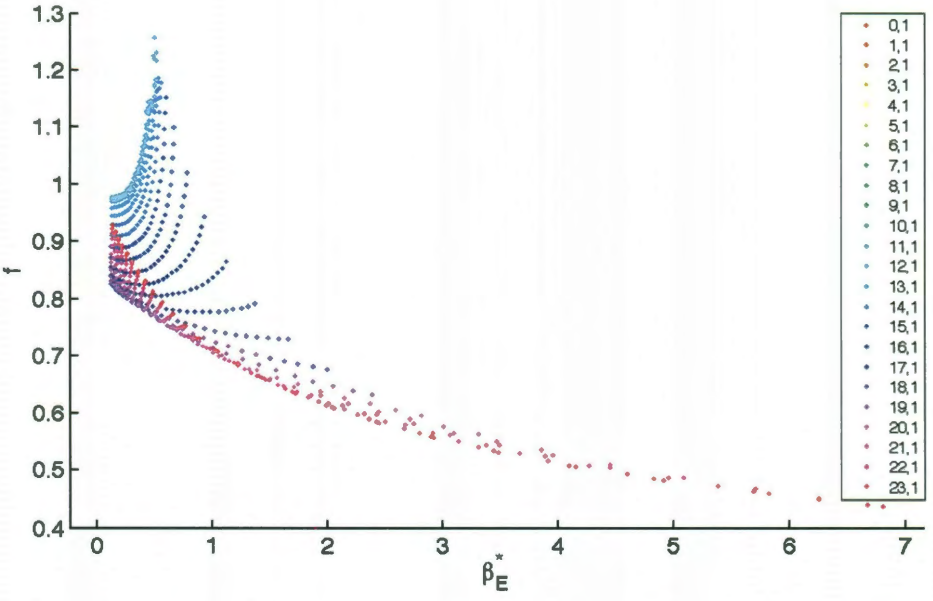

Figure 3.8 : Scatter plot of f versus β_E^* of formula (3.44) using sampling method 1. Color of the points shows different magnetic local times with 0 hour the mid-night. As β_E^* approaches to zero, the values of f do not converge to one number as in Figure 3.3 and 3.5, but exhibits a magnetic local time dependent feature. This is caused by our replacement of total B by B_z in formula (3.44).

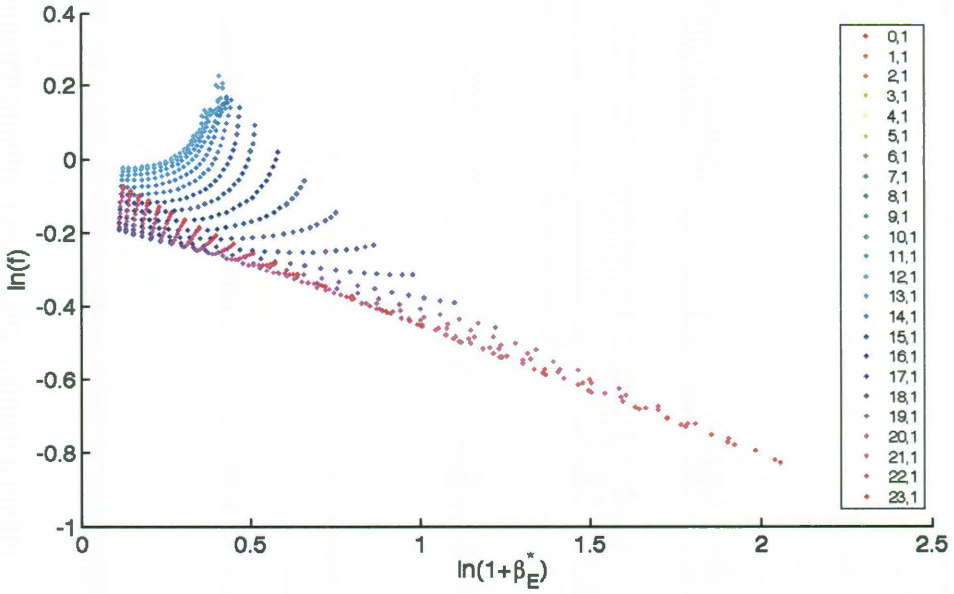

Figure 3.9 : Log-log scale plot of the result in Figure 3.8. Color of the points shows different magnetic local times with 0 hour the mid-night. The mid-night data points clearly shows a linear relation between $\ln(f)$ and $\ln(1+\beta_E^*)$, which indicates f has a power law dependence on $(1+\beta_E^*)$ in the tail. For the 2D Grad-Shafranov model, this power is $-1/2$. But the slope shown here is slightly greater than $-1/2$. Tests using other friction code results also confirm the slope value shown here.

3.10, Figure 3.11 and Figure 3.12. In these plots, data points are neatly and closely aligned, and a clear power law functional form of f on β_E^*, which is nearly independent of magnetic local time, is suggested in the log-log scale plot in Figure 3.11, despite the small deviation of the data points from local noon. Figure 3.12 shows the same plot as in Figure 3.11 except that the color contour is the ratio B_r/B_z instead of magnetic local time. From Figure 3.12, it is seen that the outlying data points have higher values of B_r/B_z than the other local-noon points. This indicates that these outlying points were from the samplings near the lower edge of the tilted GEO band in local noon, and considering that dipole tilt angle is 30°, it is unlikely that a GEO spacecraft actually samples to this location. Therefore, the different behavior of these extraneous points could be safely ignored in our estimate of the GEO flux tube volume.

In order to see how different initial conditions of the equilibrium magnetosphere may affect the alignment of the data points, a series of tests was carried out using formula (3.44). The initial conditions of these tests are listed in Table 3.3. The first row of the table represents a "basic" magnetosphere, and each of the following magnetosphere has only one parameter being different from the "basic" one. The plot of these test results are shown in Figure 3.13 through Figure 3.17. For convenience of comparisons, these figures are plotted in the same ranges of coordinates. Tests using much more disturbed initial conditions and T89 were also made and compared with the "basic" one, and those results are plotted in Figure 3.18 and Figure 3.19. In these plots, although the data points with small B_r/B_z aligned well, those with large

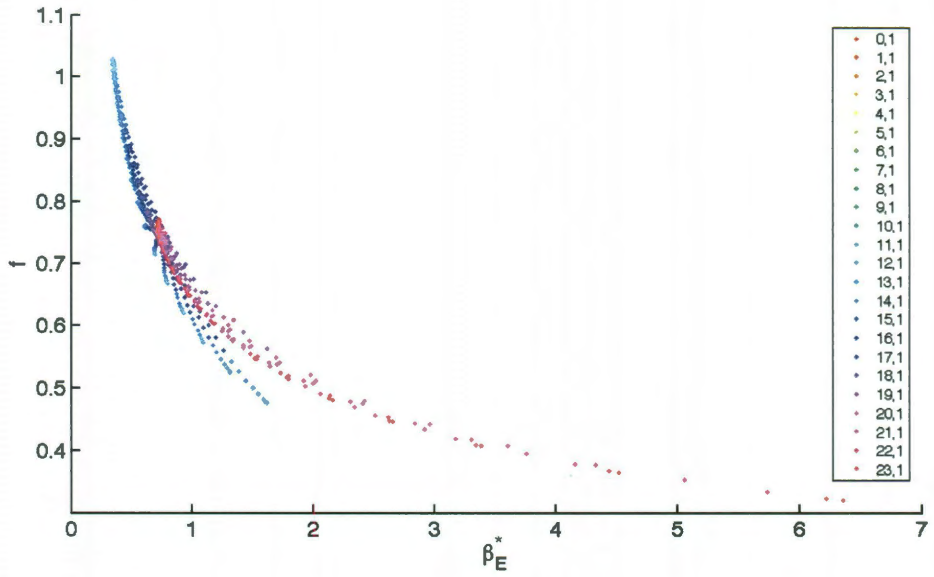

Figure 3.10 : Scatter plot of f versus β_E^* of formula (3.44) using sampling method 1. Color of the points shows different magnetic local times with 0 hour the mid-night. In contrast to Figure 3.4 and 3.6, the GEO sampled data points are neatly aligned here.

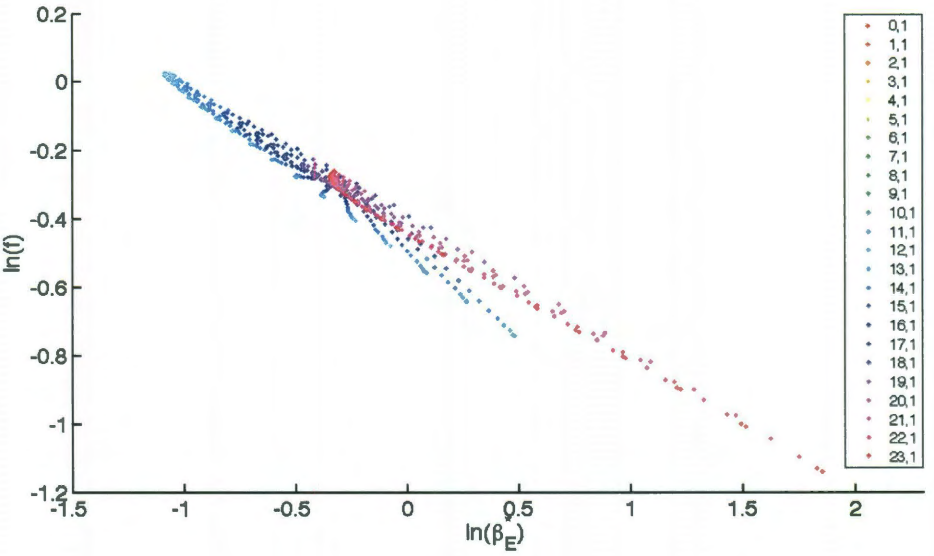

Figure 3.11 : Log-log scale plot of the result in Figure 3.10. Color of the points shows different magnetic local times with 0 hour the mid-night. The linear relation between $\ln(f)$ and $\ln(\beta_E^*)$ suggests a power law dependence of f on β_E^*.

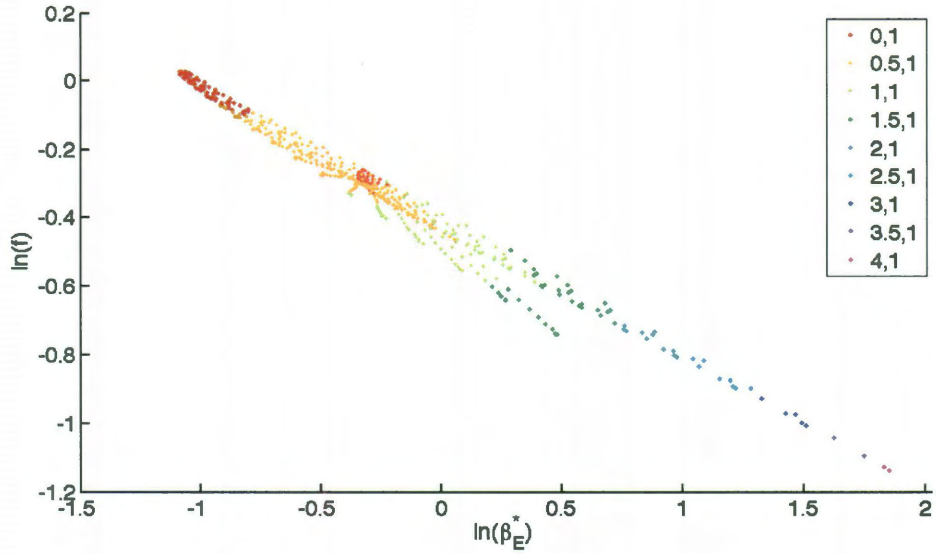

Figure 3.12 : Reproduce of Figure 3.11 with B_r/B_z as color code.

B_r/B_z had more variation. Despite that some of the highest B_r/B_z points are out of the actual GEO region, this fact still suggests that the parameter B_r/B_z must be included into our formula somehow.

3.4 Summary and future work

In this chapter, we reviewed the previous work of *Wolf et al.* [2006] [33] on the estimation of the magnetic flux tube volume in the magnetotail from *in situ* spacecraft measurements. The Wolf formula was derived from the 2D Grad-Shafranov model and calibrated by the non-tilted version of the friction code. It provides the first clue into the realistic magnetosphere from the view point of the entropy parameter (PV^{γ}), and has practical use for both the interpretation of satellite observations and

Table 3.3 : List of initial parameters used in the series of tests against (3.44)

No.\Param.	IMF B_y (nT)	IMF B_z (nT)	Dst (nT)	P_{dyn} (nPa)	tilt angle (°)
1	0	2	-20	1.5	0
2	-5	2	-20	1.5	0
3	5	2	-20	1.5	0
4	0	-5	-20	1.5	0
5	0	5	-20	1.5	0
6	0	2	-50	1.5	0
7	0	2	10	1.5	0
8	0	2	-20	3.5	0
9	0	2	-20	5.5	0
10	0	2	-20	1.5	-30
11	0	2	-20	1.5	30

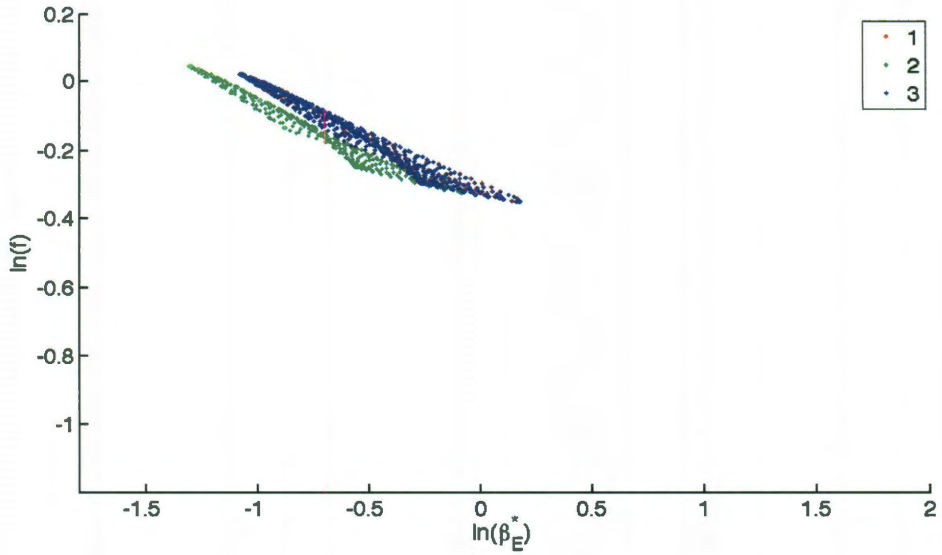

Figure 3.13 : Test of formula (3.44) for different IMF B_y. Red points (covered by blue ones) are for -5 nT IMF B_y; green points are for 0 nT IMF B_y; and blue points are for 5 nT IMF B_y. Negative and positive IMF B_y's have the same effect.

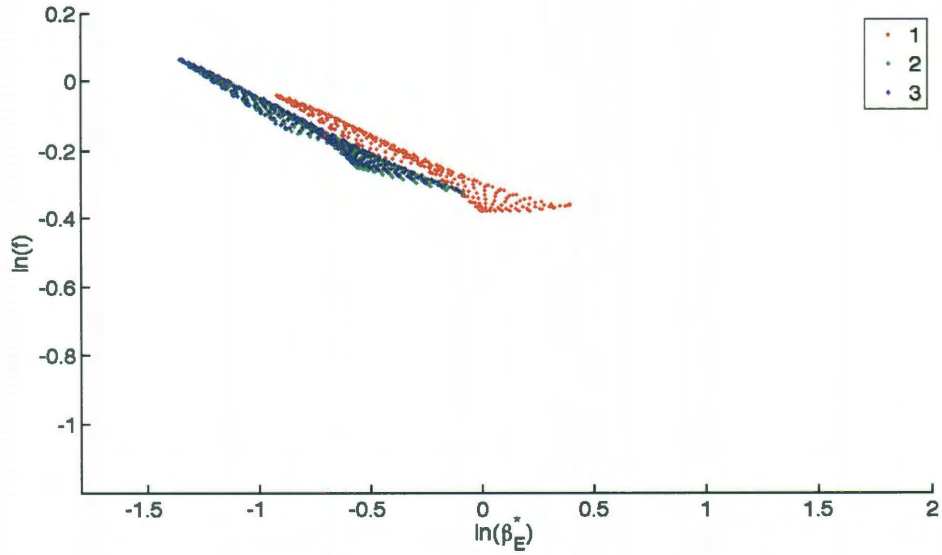

Figure 3.14 : Test of formula (3.44) for different IMF B_z. Red points are for -5 nT IMF B_z; green points (covered by blue ones) are for 2 nT IMF B_z; and blue points are for 5 nT IMF B_z. Northward IMF B_z does not have an effect; southward IMF B_z does.

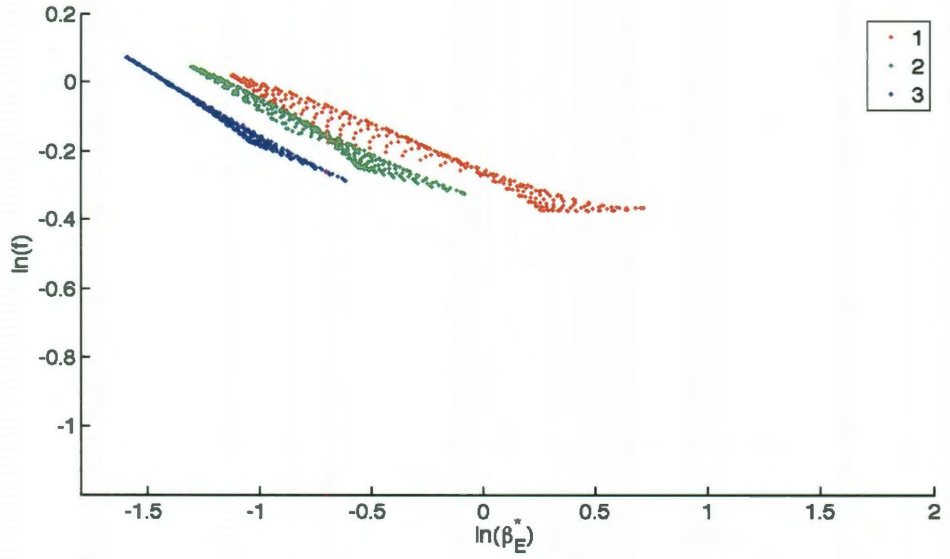

Figure 3.15 : Test of formula (3.44) for different Dst. Red points are for -50 nT Dst; green points are for -20 nT Dst; and blue points are for +10 nT Dst.

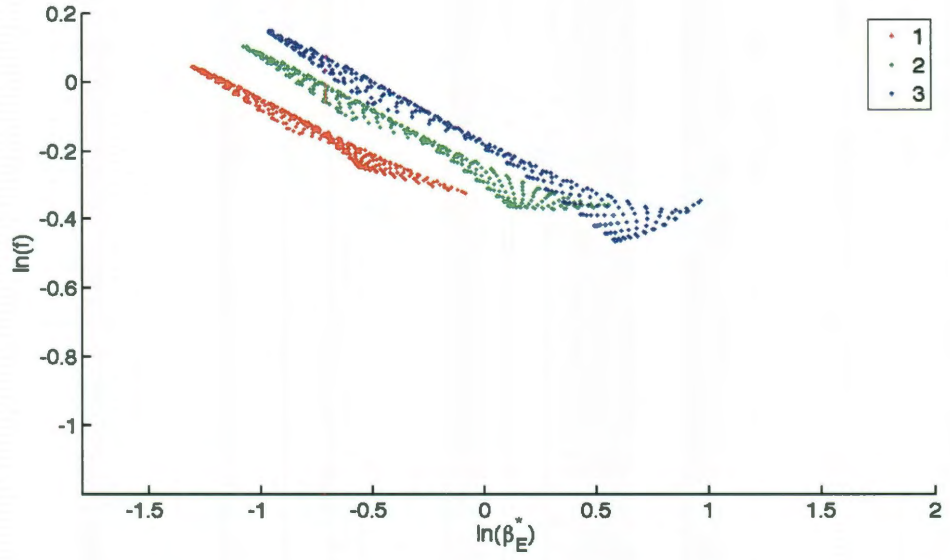

Figure 3.16 : Test of formula (3.44) for different P_{dyn}. Red points are for 1.5 nPa P_{dyn}; green points are for 3.5 nPa P_{dyn}; and blue points are for 5.5 nPa P_{dyn}.

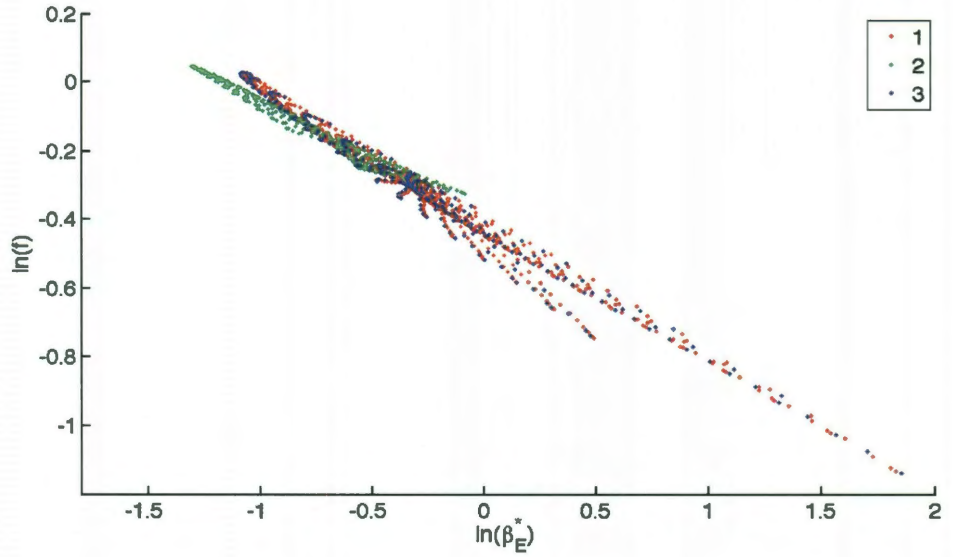

Figure 3.17 : Test of formula (3.44) for different dipole tilt angles. Red points are for $-30°$ tilt angle; green points are for $0°$ tilt angle; and blue points are for $30°$ tilt angle.

development of plasma sheet convection theories. However, tests of the Wolf formula against more realistic magnetospheres calculated by the new version of the friction code reveal that its prediction becomes poorer as tilt angle becomes larger. Therefore, a generalized Wolf formula is desired that takes account of dipole tilt and probably other parameters, such as the IMF or the dynamic pressure.

In the pursuit of this generalized Wolf formula, we generalized in section 3.2 the theory for calculating flux tube volume under the tail configuration. These generalizations included corrections to the plasma pressure, B_y component and the dipole tilt angle.

Moreover, the abundance of GEO spacecraft also requires that we develop a flux tube volume estimate for that region. Clearly, the Wolf formula is not applicable

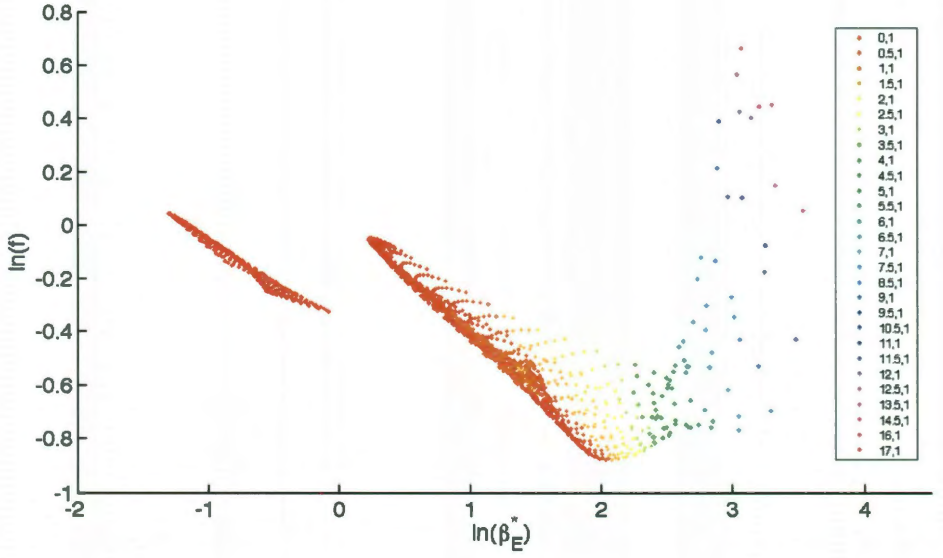

Figure 3.18 : Test of formula (3.44) with disturbed conditions in T96. These initial conditions are: 20° tilt angle, -7 nT IMF B_y, -7 nT IMF B_z, -20 nT Dst, 5.0 nPa P_{dyn}, and K_p 6 for the Spence-Kivelson pressure model. The shorter line on the left is the "basic" line, and the longer on the right is comprised from data points of the disturbed test. Color shows values of B_r/B_z.

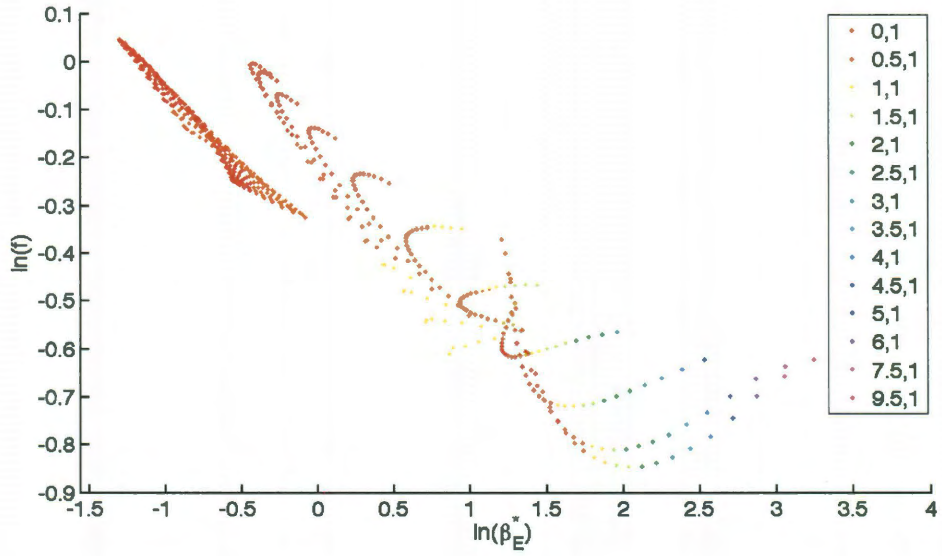

Figure 3.19 : Test of formula (3.44) with disturbed conditions in T89. These initial conditions are: 20° tilt angle, -7 nT IMF B_y, -7 nT IMF B_z, K_p 5, and 5.0 nPa P_{dyn}. The shorter line on the left is the "basic" line, and the longer on the right is comprised from data points of the disturbed test. Color shows values represent B_r/B_z.

there because it was derived in the tail configuration. In section 3.3, we have found an empirical approach to estimate the flux tube volume at GEO distance based on a correction to the dipole flux tube volume by the finite plasma β. The empirical method presented by equation (3.44) has exhibited promising attributes in determining a formula that incorporates some of the geo-activity parameters, but the final form of the factor f still remains unclear. From the discussion in section 3.3, the following work on the GEO flux tube volume focuses on making use of the parameter B_r/B_z to determine the functional form of f, and calibrating it against equilibrated magnetospheres in the friction code.

Finally, currently operating GEO satellites may not measure the full suite of physical quantities needed our estimate. For instance, the LANL GEO spacecraft measure the plasma distribution function [*McComas et al.*, 1993 [23]], from which thermal pressure and the direction of magnetic field can be derived, but the magnitude of B is unknown; the GOES spacecraft have magnetometer but can not measure pressure. Therefore, how can we make compromise given these limitations in measurement should be another direction for future work.

Chapter 4

Summary, Conclusions and Future Work

In this dissertation, we have addressed mathematically the general magnetospheric equilibrium problem, described the numerical algorithm called the friction code to calculate the 3D magnetosphere equilibrium state with arbitrary Earth dipole tilt and interplanetary magnetic field (IMF) polarity, and discussed the ongoing work of looking for an estimate of the flux tube volume at the geosynchronous orbit (GEO) as one application of the friction code.

Chapter 1 started from the magnetohydrodynamic (MHD) equations, which describe the large scale space plasma convection, and under the slow flow assumption (that is, flow speed is much smaller than Alfvén wave speed), we derived the system of equations describing the magnetohydrostatic equilibrium. The equilibrated configuration of the magnetosphere is of great importance in the sense that it determines field aligned currents of the system through Vasyliunas equation, thus constitutes an essential link in the loop of the magnetosphere-ionosphere coupling (as shown in Figure 1.2). Analytical treatments of the problem, namely the Grad-Shafranov equation and the 3D asymptotic magnetotail theory, are only available and solvable under symmetry constraints and certain simplifications. Therefore, numerical algorithms have been developed to calculate the equilibrium state in more realistic configurations. The MAG-3D code and the friction code are the only two major numerical

applications available today.

In Chapter 2, we described the algorithms of the dipole-tilted friction code. By examining the system's kinetic energy and potential energy, and the force-imbalance density, we have demonstrated that the new version of the friction code is able to consecutively transform the potential energy into kinetic energy, dissipate the latter by artificial friction, and thereby reduce the force imbalance of the system to less than 1/10 of its initial value of a magnetospheric configuration with arbitrary dipole tilt angle and IMF polarity. The finite residual force imbalance might be a result of our finite grid resolution, and therefore is intrinsic of the friction code algorithm. To further reduce the force imbalance, coupling the friction code with the MAG-3D code might yield better force balance.

In addition, we also discussed the ongoing work of the PV^{γ} correction that is intentionally designed to attenuate the numerical diffusion inherent of the third order Adams-Bashforth equation solver. The PV^{γ} correction does not work well in all instances. To better assess the effectiveness of the PV^{γ} correction, especially its ability to prevent the tearing mode instability from developing, more thorough tests need to be done in the future. The difficulty is, on one hand, due to the large amount of field line tracings involved in it, the PV^{γ} correction is computationally expensive; on the other hand, we do not know at approximately what "time" during the relaxation procedure that the numerical diffusion becomes critical and field line reconnection starts. Therefore, these tests suggest that the PV^{γ} correction should be called often

and/or a smart guess on the time point. In addition, the successful implementation of the PV^{γ} correction also depends crucially on the accuracy of the field line tracer. To date, we have not found any better field line tracer that is more accurate and robust than the one we are currently using. Under such situations, adding a convergence test to the field line tracing might be a probable solution. For the field line tracing of one grid node, instead of doing it once, we repeat the tracing for many times by reducing the error tolerance every time, and see whether the ionospheric footprints and the flux tube volume integrations converge. If they converge to fixed location and value during this procedure, we then have a sense of what is the proper error tolerance to obtain accurate field line tracing. We may be able to extrapolate the convergence sequence to obtain the accurate footprints and flux tube volume. However, in this case, the PV^{γ} correction could become even more expensive.

A detailed review of the current status of the magnetic flux tube volume estimates was given in Chapter 3. Following that, we generalized the analytical calculation of the flux tube volume into more complicated magnetotail configurations. From these generalizations, we concluded that in the magnetotail, flux tube volume calculations have the features that: 1) they are inversely proportional to the 1/2 power of the total pressure; 2) they are proportional to some tailward characteristic length; and 3) far from the Earth, dipole tilt does not make an explicit effect. These calculations are the only tractable theoretical tools that are available through my research of the literature. They represent our attempt to find an improvement of the Wolf formula to

incorporate the dipole tilt and IMF as its input parameters, since it is often applied not so far from the Earth where the effect of dipole is not negligible. Although those calculations may not be directly used onto the Wolf formula, they nonetheless provided a guidance to the possible future improvement.

We also studied the flux tube volume estimation for the inner edge of the plasma sheet at geosynchronous orbit. In spite of its practical necessity in exploiting the data collected by GEO spacecraft, the GEO flux tube volume behavior may also give us clue on how to extrapolate the Wolf formula nearer to the Earth. Based on a modified calculation of the dipolar shape flux tube volume, we have found a promising way to estimate the flux tube volume at GEO by a correction from the local plasma β parameter. Future effort of this work is certainly focused on determining the concrete functional form of the factor f and calibrating empirical parameters therein. Among the various guesses of the form of f, the following one might be suitable

$$f = \frac{C}{\sqrt{1 + \kappa\beta_E^*}} \tag{4.1}$$

where C and κ are functions of the IMF, Dst and dynamic pressure. The square root in (4.1) clearly characterizes the β dependence in the tail configuration, hence in the far tail, where β is much greater than unity, the $g^2(\theta)$ factor in β_E^* will cancel out with the $g(\theta)$ appeared in formula (3.44), which says that the flux tube volume has no explicit tilt angle dependence. κ is a character of the dipole, thus shall reduce to one as the effect of dipole is negligible. Among those initial parameters, Dst certainly has an influence on the effective dipole moment, therefore, κ would be at least dependent

on Dst. C is a scale of the characteristic length. IMF B_z and dynamic pressure both affect the characteristic length in the sense that, when the dayside characteristic length is increased by either the corrosion of the increased southward IMF B_z or the decline of the dynamic pressure, the characteristic length on the nightside decreases because of either enhanced flux convection or reduced frictional drag of the solar wind respectively. Therefore, the functional appearance of IMF B_z and dynamic pressure in C will be accompanied by the factor of $\cos(\phi)$, where ϕ is the magnetic local time. Of course, these wild guesses need to be tested against the friction code generated magnetospheres.

Last but not least, our GEO band used to sample the GEO spacecraft positions can be refined to only cover the exact envelope of the possible orbits when the dipole tilt is non-zero. This will help us rule out the off trend data points with the highest B_r/B_z values and thereby yield the best parameter calibration.

Appendix A

Wolf and Sazykin's discussion on the use of ghost cells and the Dirichlet boundary condition

This appendix is presented based on *Wolf*'s personal correspondence to the author. The correspondence started from a discussion on the friction code boundary condition for velocities: whether it is over restricted to specify the Dirichlet boundary condition and the anti-symmetric ghost cell values simultaneously. Below is *Wolf*'s original writing with a minimal revision.

For simplicity of analysis, consider just linear sound waves propagating in the x-direction, in a plasma that has a uniform magnetic field in the x-direction. If a set of boundary conditions is valid in the general case, it should be valid in this specific simple case. The geometry is shown below. Points 2 and 5 are boundary points, 1 and 6 are ghost points, and 3 and 4 are inside the modeling region.

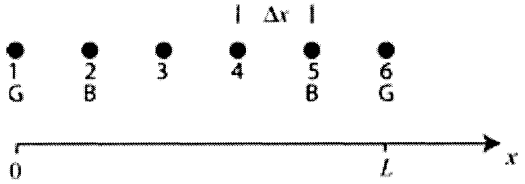

Figure A.1 : Numerical grid of a 1D media.

Because we are considering just linear sound waves traveling in the x-direction,

we write continuity and momentum equations in the form

$$\frac{\partial \delta\rho}{\partial t} + \rho \frac{\partial \delta v}{\partial x} = 0 \tag{A.1}$$

$$\rho \frac{\partial \delta v}{\partial t} + c_s^2 \frac{\partial \delta\rho}{\partial x} = 0 \tag{A.2}$$

where $c_s^2 = \gamma P/\rho$, and we have already used the energy equation $\delta P/P = \gamma \delta\rho/\rho$. For points $j = 2, 3, 4, 5$, we apply these differential equations in the simple difference forms

$$\frac{\delta\rho(j) - \delta\rho_o}{\Delta t} + \rho \frac{\delta v(j) - \delta v_o(j)}{2\Delta x} = 0 \tag{A.3}$$

$$\rho \frac{\delta v(j) - \delta v_o}{\Delta t} + c_s^2 \frac{\delta\rho(j) - \delta\rho_o(j)}{2\Delta x} = 0 \tag{A.4}$$

where the subscript "o" represents the value at the previous time step. The boundary conditions in the friction code's manner are

$$\delta\rho(1) = \delta\rho(3), \quad \delta\rho(6) = \delta\rho(4), \quad \delta\rho(2) = \delta\rho_o(2), \quad \delta\rho(5) = \delta\rho_o(5) \tag{A.5}$$

$$\delta v(1) = -\delta v(3), \quad \delta v(6) = -\delta v(4), \quad \delta v(2) = 0, \quad \delta v(5) = 0 \tag{A.6}$$

Now let's count algebraic equations. Equations (A.3) and (A.4) applied at 4 grid points each amounts to 8 equations, and boundary conditions (A.5) and (A.6) amount to 8 more equations, making a total of 16 equations. There are 12 unknowns ($\delta\rho(1), \ldots, \delta\rho(6)$, $\delta v(1), \ldots, \delta v(6)$). Therefore, we would naively think that the 12 unknowns are over-specified.

Physical example:

We know some analytic solutions to (A.1) and (A.2) assuming zero velocity at the end points. One possibility is the fundamental standing-wave solution

$$\delta v = C \sin\left(\frac{\pi x}{L}\right) \cos\left(\frac{\pi c_s t}{L}\right) \tag{A.7}$$

Substituting (A.7) in (A.1) and integrating from $t = 0$ to the present time gives

$$\delta\rho(x,t) = \delta\rho(x,0) - \frac{\rho C}{c_s} \cos\left(\frac{\pi x}{L}\right) \sin\left(\frac{\pi c_s t}{L}\right) \tag{A.8}$$

Substituting (A.7) and (A.8) in (A.2) gives

$$\delta\rho(x,0) = 0$$

so that

$$\delta\rho(x,t) = -\frac{\rho C}{c_s} \cos\left(\frac{\pi x}{L}\right) \sin\left(\frac{\pi c_s t}{L}\right) \tag{A.9}$$

Note that this simple standing wave does not satisfy the condition that density is constant in time at the end points $x = 0$ and L, unless the wave amplitude C is zero. Specifying both density and velocity at the end points would seem to be over-specifying the problem.

Concluding comment:

From the point of view of counting equations and unknowns, suppose that we want to specify zero velocity at the end points and we want to use ghost cells. Then we should not specify $\delta\rho(2)$ and $\delta\rho(5)$ as boundary conditions. Furthermore the ghost-cell conditions $\delta v(1) = -\delta v(3)$ and $\delta v(6) = -\delta v(4)$ imply that $\delta v(2) \approx \delta v(4) \approx 0$, so that we shouldn't specify all of those conditions. That would imply an elimination of 4 equations and bring the number of equations and unknowns back into balance.

Bibliography

[1] I. B. Bernstein, E. A. Frieman, M. D. Kruskal, and R. M. Kulsrud, *An energy principle for hydromagnetic stability problems*, Proc. R. Soc., Ser. A, no. 244, 1958, pp. 17–40.

[2] J. Birn, *Self-consistent magnetotail theory: general solution for the quiet tail with vanishing field-aligned currents*, Journal of Geophysical Research **84** (1979), no. A9, 5,143–5,152.

[3] J. Birn, *Magnetotail equilibrium theory: the general three-dimensional solution*, Journal of Geophysical Research **92** (1987), no. A10, 11,101–11,108.

[4] J. Birn, *Three-dimensional equilibria for the extended magnetotail and the generation of field-aligned current sheets*, Journal of Geophysical Research **94** (1989), no. A1, 252–260.

[5] J. Birn, *The distortion of the magnetotail equilibrium structure by a net cross-tail magnetic field*, Journal of Geophysical Research **95** (1990), no. A6, 8,019–8,028.

[6] J. Birn, M. Hesse, K. Schindler, and S. Zaharia, *Role of entropy in magnetotail dynamics*, Journal of Geophysical Research **144** (2009), no. A00D03.

[7] J. Birn, R. Sommer, and K. Schindler, *Open and closed magnetospheric tail configurations and their stability*, Astrophysics and Space Science **35** (1975), 389–402.

[8] J. Birn, R. Sommer, and K. Schindler, *Self-consistent theory of the quiet magnetotail in three dimension*, Journal of Geophysical Research **82** (1977), no. 1, 147–154.

[9] C. Canuto, M. Y. Hussaini, A. Quarteroni, and T. A. Zang, *Spectral methods in fluid dynamics*, Springer-Verlag, New York, 1988.

[10] Anthony A. Chan, Mengfen Xia, and Liu Chen, *Anisotropic Alfvén-ballooning modes in Earth's magnetophsere*, Journal of Geophysical Research **99** (1994), no. A9, 17,351–17,366.

[11] C. X. Chen and R. A. Wolf, *Interpretation of high-speed flows in the plasma sheet*, Journal of Geophysical Research **98** (1993), no. A12, 21,409–21,419.

[12] C. Z. Cheng, *Three-dimensional magnetospheric equilibrium with isotropic pressure*, Geophysical Research Letters **22** (1995), no. 7, 2401–2404.

[13] R. Chodura and A. Schlüter, *A 3D code for MHD equilibrium and stability*, Journal of Computational Physics **41** (1981), 68–88.

[14] R. E. Denton and Y. Hu, *Symmetry boundary conditions*, Journal of Computational Physics **228** (2009), 4,823–4,835.

[15] J. P. Freidberg, *Ideal magnetohydrodynamic theory of magnetic fusion systems*, Review of Modern Physics **54** (1982), no. 3, 801–902.

[16] L.-N. Hau, *Effects of steady state adiabatic convection on the configuration of the near-Earth plasma sheet, 2*, Journal of Geophysical Research **96** (1991), no. A4, 5591–5596.

[17] Michael Hesse and Joachim Birn, *Three-dimensional magnetotail equilibria by numerical relaxation techniques*, Journal of Geophysical Research **98** (1993), no. A3, 3973–3982.

[18] Robert V. Hilmer and Gerd-Hannes Voigt, *The effects of a magnetic B_y component on geomagnetic tail equilibria*, Journal of Geophysical Research **92** (1987), no. A8, 8660–8672.

[19] Margaret G. Kivelson and Christopher T. Russell (eds.), *Introduction to space physics*, Cambridge University Press, New York, 1995.

[20] H. Korth, M. F. Thomsen, J. E. Borovsky, and D. J. McComas, *Plasma sheet access to geosynchronous orbit*, Journal of Geophysical Research **104** (1999), no. A11, 25,047–25,061.

[21] Sergei I. Krasheninnikov, Peter J. Catto, and R. D. Hazeltine, *Magnetic dipole equilibrium solution at finite plasma pressre*, Physical Review Letters **82** (1999), no. 13, 2689–2692.

[22] Colby Lemon, Frank Toffoletto, Michael Hesse, and Joachim Birn, *Computing magnetospheric force equilibria*, Journal of Geophysical Research **108** (2003), no. A6.

[23] D. J. McComas, S. J. Bame, B. L. Barraclough, J. R. Donart, R. C. Elphic, J. T. Gosling, M. B. Moldwin, K. R. Moore, and M. F. Thomsen, *Magnetospheric plasma analyzer: Initial three-spacecraft observations from geosynchronous orbit*, Journal of Geophysical Research **98** (1993), no. A8, 13,453–13,465.

[24] S. Sazykin, *Theoretical studies of penetration of magnetospheric electric fields to the ionosphere*, Ph.D. thesis, University of Utah, 2000.

[25] Harlan E. Spence, Margaret G. Kivelson, and Raymond J. Walker, *Magnetospheric plasma pressures in the midnight meridian: Observations from 2.5 to 35 R_E*, Journal of Geophysical Research **94** (1989), no. A5, 5264–5272.

[26] N. A. Tsyganenko, *A magnetospheric magnetic field model with a warped tail current sheet*, Planet. Space Sci. **37** (1989), no. 1, 5–20.

[27] N. A. Tsyganenko and T. Mukai, *Tail plasma sheet models derived from Geotail particle data*, Journal of Geophysical Research **108** (2003), no. A3.

[28] N. A. Tsyganenko and D. P. Stern, *Modeling the global magnetic field of the large-scale birkeland current systems*, Journal of Geophysical Research **101** (1996), no. A12, 27,187–27,198.

[29] Vytenis M. Vasyliunas, *Mathematical models of magnetospheric convection and its coupling to the ionosphere*, Particles and Fields in the Magnetosphere (Hingham, MA) (B. M. McCormac, ed.), D. Reidel, 1970, pp. 60–71.

[30] G.-H. Voigt and R. A. Wolf, *On the configuration of the polar cusps in earth's magnetosphere*, Journal of Geophysical Research **90** (1985), no. A5, 4046–4054.

[31] G.-H. Voigt and R. A. Wolf, *Quasi-static magnetospheric MHD processes and the "ground state" of the magnetosphere*, Reviews of Geophysics **26** (1988), no. 4, 823–843.

[32] Gerd-Hannes Voigt, *Magnetospheric equilibrium configurations and slow adiabatic convection*, Solar Wind-Magnetosphere Coupling (Y. Kamide and J. A. Slavin, eds.), Terra Scientific Publishing Company, 1986, pp. 233–273.

[33] R. A. Wolf, V. Kumar, F. R. Toffoletto, G. M. Erickson, A. M. Savoie, C. X. Chen, and C. L. Lemon, *Estimating local plasma sheet $PV^{5/3}$ from single-spacecraft measurements*, Journal of Geophysical Research **111** (2006), no. A12218.

[34] R. A. Wolf, Yifei Wan, X. Xing, J.-C. Zhang, and S. Sazykin, *Entropy and plasma sheet transport*, Journal of Geophysical Research **114** (2009), no. A00D05.

[35] Richard A. Wolf, *Physics of the magnetosphere*, textbook draft used at Rice University, to be published by Cambridge University Press.

[36] X. Xing and R. A. Wolf, *Criterion for interchange instability in a plasma connected to a conducting ionosphere*, Journal of Geophysical Research **112** (2007), no. A12209.

[37] J. Yang, F. R. Toffoletto, G. M. Erickson, and R. A. Wolf, *Superposed epoch study of $PV^{5/3}$ during substorms, pseudobreakups and convection bays*, Geophys. Res. Lett. **37** (2010), no. L07102.

[38] S. Zaharia, C. Z. Cheng, and K. Maezawa, *3-D force-balanced magnetospheric configurations*, Annales Geophysicae **22** (2004), 251–265.

[39] Sorin Zaharia and C. Z. Cheng, *Can an isotropic plasma pressure distribution be in force balance with the T96 model field?*, Journal of Geophysical Research **108** (2003), no. A11, 1412.